The role of sensible heating in enhancing cloud formation over forest

MSc-thesis by Peter Bosman

Supervisor:

Chiel van Heerwaarden

July 2017

The role of sensible heating in enhancing cloud formation over forest

MSc-thesis at Meteorology and Air Quality Group,

Wageningen University, Wageningen

Author: Peter Bosman

Registration nr.: 901219109050

Supervisor:

Chiel van Heerwaarden

Examiner:

Bert Holtslag

31 July 2017

Abstract

In a recent study from Teuling et al. [*Nature Communications,* 8 (2017)], it was shown for two forests (Les Landes and Sologne) in France that summer cloud cover is increased over the forest compared to its surroundings. This study aims to contribute to the elucidation of the physical mechanisms responsible for this increase in cloud cover, focusing on surface flux partitioning differences. This was done by performing a case study for a heatwave day on which enhanced cloud cover over the forest of Les Landes was visible on satellite images (17 July 2006). Two numerical experiments (large eddy simulations) with a homogeneous forest cover were performed, one in which the sensible heat flux was increased with approximately 5% of the net radiation and another one in which the same amount of energy was added to the latent heat flux. The addition of energy to the sensible heat flux led to a stronger increase in cloud cover than the same addition to the latent heat flux. The mean relative humidity at the boundary layer top was similar, showing it was not sufficient as indicator for cloud formation in this case. Analysis of the (bimodal) relative humidity probability density distribution revealed differences in the shape of the distribution, the number of cells close to saturation was slightly higher in the run with the enhanced sensible heat flux. An important reason for the differences in cloud cover between the experiments was found to be the boundary layer warming associated with the stronger sensible heat flux, which decreases the required amount of energy for air parcels to reach the lifting condensation level. As forests in the region do have a higher sensible heat flux, we highlighted a potential mechanism for enhanced cloud cover, but its importance remains to be quantified.

Table of Contents

1 Introduction

Forests are of crucial importance regarding climate change by forming large carbon stores, approximately 800 billion tons of carbon is stored in forest trees and underlying soils (Brown, 1998; as cited by Sohngen & Mendelsohn, 2003). Forests are also known to influence climate by impacting the water and energy balance of the land surface (Bonan, 2008; Beringer et al., 2005). A thorough understanding of the interactions between forests and the overlying atmosphere is therefore crucial to make accurate climate predictions in the context of climate change. This knowledge is also crucial to predict the effects of forest clearance or afforestation.

Out of the broad range of forest-atmosphere interactions, this thesis study will focus on the effect of forests on cloud cover. These effects are still poorly understood (Teuling et al., 2017), despite the fact that the presence of clouds has a large influence on the local climate by altering the radiation balance.

Several studies have investigated the relation between the presence of forest and cloud cover using satellite observations. Many of these studies focus on the Amazon area (e.g. Durieux et al., 2003; Wang et al., 2009; Negri et al., 2004). Durieux et al. (2003) report (for the dry season) increased low level cloudiness in the early afternoon, but less convection at night and in the early morning for deforested areas compared to forested areas. Wang et al. (2009) found a preference for shallow clouds to occur over deforested areas. Negri et al. (2004) found (for the dry season) both shallow cumulus cloudiness and deep convection cloudiness to be higher over deforested areas compared to dense forest areas. For the lowlands in northern Costa Rica, Nair et al. (2003) found suppressed late morning cumulus cloudiness over deforested areas compared to forested areas, during the dry season. Gambill & Mecikalski (2011) found for the south-eastern United States that in summer convective clouds are more likely to develop over forest. Teuling et al. (2017) used satellite observations to investigate the relation between the presence of forest and cloud cover for two forest areas in France (Les Landes and Sologne). They found clear evidence of an increase in summer cloud cover over forested areas.

These contrasting results stress the importance of getting a thorough understanding of the mechanisms behind cloud formation over forests. Several mechanisms and processes have been suggested to determine differences in cloud cover between forest areas and their surroundings, they are shortly discussed here and are summarised in Figure 1.

Surface energy balances are different between forest and grassland (Teuling et al., 2010). Forests have a lower albedo than their surroundings (Bonan, 2008), this leads to more energy that is available at the earth's surface (Teuling et al., 2017). This energy can be used for evapotranspiration or for warming the atmosphere. The extra energy, together with differences in partitioning between evapotranspiration and warming the atmosphere (Teuling et al., 2010) leads to differences in the sensible (H) and latent (LE) heat fluxes. This in turn might lead to differences in cloud formation (Gentine et al., 2013; Ek & Mahrt, 1994; Ek & Holtslag, 2004; Huang & Margulis, 2011). One of the ways in which this might happen is by modifying the height of the lifting condensation level and the boundary layer top. The height of the boundary layer top also influences the temperature at the top of the boundary layer, which is relevant for cloud formation as well (Ek & Mahrt, 1994).

Another difference is that forests have a rougher canopy (Mahrt & Ek, 1993), stimulating a more efficient exchange of heat and momentum with the atmosphere (Teuling et al., 2017), compared to a land cover with a less rough canopy such as grassland. This efficient exchange also has the consequence that the same amount of heat transport to the atmosphere can take place with a lower surface temperature (Teuling 2017), thereby reducing outgoing longwave radiation. This contributes to the extra amount of energy that is available at the surface. Shannak et al. (2011) found drag forces over forest that were three orders of magnitude larger than those over grass. The slowing down of air masses due to roughness also causes frictional convergence (Teuling et al., 2017), i.e. when the leading part of an air mass experiences more drag from the surface than the trailing part of the air mass (and is thus slowed down more), convergence occurs. The mass continuity principle requires in these cases that air will be lifted (American Meteorological Society, 2012). This lifting of air may also be relevant for cloud formation.

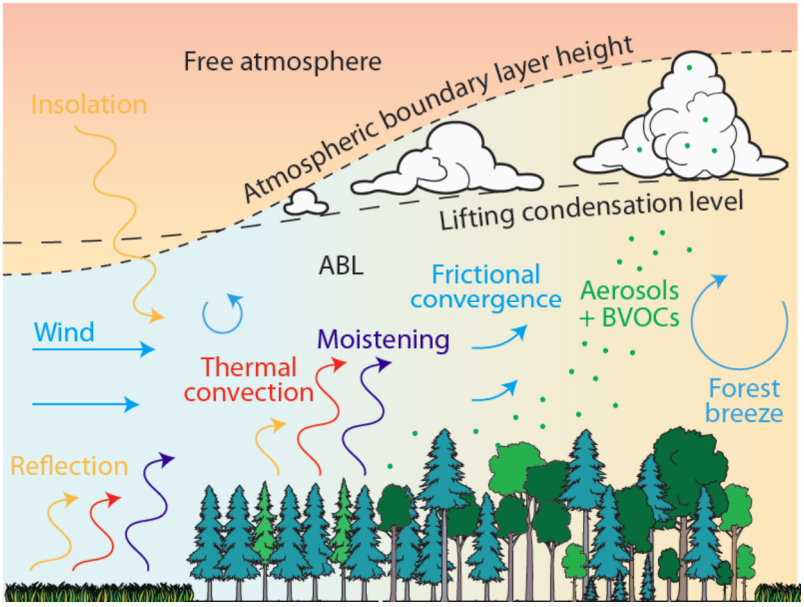

Figure 1: Important processes and mechanisms for cloud formation, which might differ between forest and surroundings (size of arrows differs). ABL stands for atmospheric boundary layer, BVOC for biogenic volatile organic compound. The orange colour relates to radiation, red to transport of heat, purple to moisture and blue to wind. Taken from Teuling et al. (2017)

The creation of mesoscale circulations due to heterogeneities in land cover is mentioned in several studies (Wang et al., 2009; Teuling et al., 2017; Gambill & Mecikalski, 2011). A difference in temperature between a forest and a non- forest area might lead to a convective circulation between the two areas (Souza et al., 2000), similar to the formation of a sea breeze. Another mechanism involves the emission of volatile organic compounds, which enhances the amount of cloud condensation nuclei in the atmosphere (Spracklen et al., 2008).

Several modelling efforts have been undertaken to predict the effects of forest on regional climate, but many studies do not explicitly report effects on cloud cover. Many of these simulations were done with coupled land surface & general circulation models (e.g. Shukla et al., 1990; Costa & Foley, 2000), which are hydrostatic and do not explicitly solve convection. Large eddy simulation (LES) has also been applied to forests (e.g. Eder et al., 2015; Shaw & Schumann, 1992; Cassiani et al., 2008), but these studies often do not consider cloud formation. Eder et al. (2015) made use of LES to investigate the presence of mesoscale circulations for a forest in Israel surrounded by a semi-arid, very sparsely vegetated region. The difference between the forest and the surroundings was modelled by a difference in roughness lengths and surface fluxes. A simulation without background wind produced a mesoscale circulation. The study did not include the effects of this on cloud cover. Garcia-Carreras et al. (2011) and Garcia-Carreras & Parker (2011) applied 2D LES to look deeper into the mesoscale circulations induced by land cover differences; this was modelled by varying the partitioning between the

surface fluxes. Their results provide insights in the development of mesoscale circulations, including the effects on cloudiness (Garcia-Carreras et al., 2011) and on rainfall (Garcia-Carreras & Parker, 2011).

From the broad array of involved processes mentioned before, this study focuses on the direct effects (not via potentially induced mesoscale circulations) of differences in flux partitioning between the sensible and latent heat flux. We performed a case study for a forest in the southwest of France (Les Landes). This is a planted maritime pine (*Pinus pinaster*) forest which has an area of thousands of square kilometres. For this forest, Teuling et al. (2017) showed enhanced cloud cover over the forest compared to its surroundings in summer. This forest is part of the FLUXNET (Baldocchi et al., 2001) sites. Teuling et al. (2010) showed, using FLUXNET observations, that for West and Central Europe forests have a higher net radiation and sensible heat flux than grassland and cropland. They also showed that these differences increase during the initial (non soil moisture limited) stages of a heatwave. We therefore performed a case study for a heatwave day on which enhanced cloud cover was visible on satellite images, using large eddy simulation.

This study aims to gain more understanding of how flux partitioning differences influence cloud formation. Thereby we contribute to the overall question of why Western European forests seem to have enhanced cloud cover. The research questions are set up as follows:

1) How do changes in flux partitioning alter cloud formation?
2) To what extent can differences in flux partitioning explain the enhanced cloud cover over forest compared to its surroundings?

The first research question represents the bulk of this research, the second research question frames the finding of the first in the context of the overall question of why Western European forests seem to have enhanced cloud cover.

2 Methodology

A case study was performed using large eddy simulation (LES) for a day on which enhanced cloud cover over forest was visible on satellite images. The case is described in section 2.1, thereafter the applied model is described (section 2.2). The model configuration is dealt with in section 2.3. Section 2.4 explains the numerical experiments which were performed, some frequently used variables in our analysis are explained in section 2.5.

2.1 Case description

The selected day was 17 July 2006. On this day, there was a clear difference in cloud cover between the forest of Les Landes and the surroundings visible in the satellite images (Figure 2). Heat wave conditions prevailed in the region by this time (Pascal et al., 2012). The mean sea level pressure chart obtained from ERA-Interim data (some information about this dataset

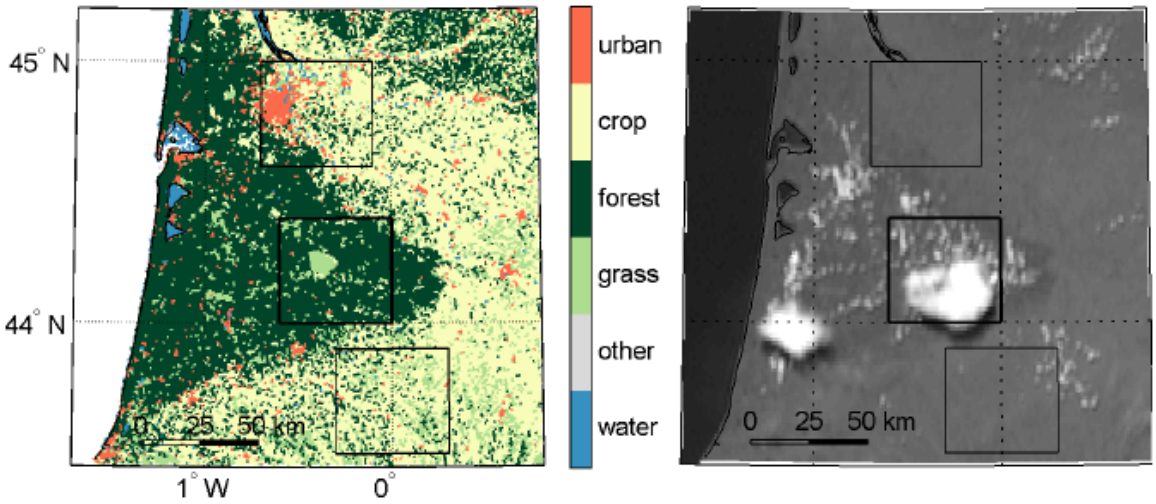

Figure 2: Land use map of the region encompassing the forest of Les Landes (left) and satellite image (Meteosat Second Generation channel 12) of 17 July 2006 at 15 LT (right) of the same area. The enhanced cloud cover over the forest is clearly visible. The thick black square encompasses a forest area, the thin squares non-forest areas. Figures copied from Teuling et al., 2017.

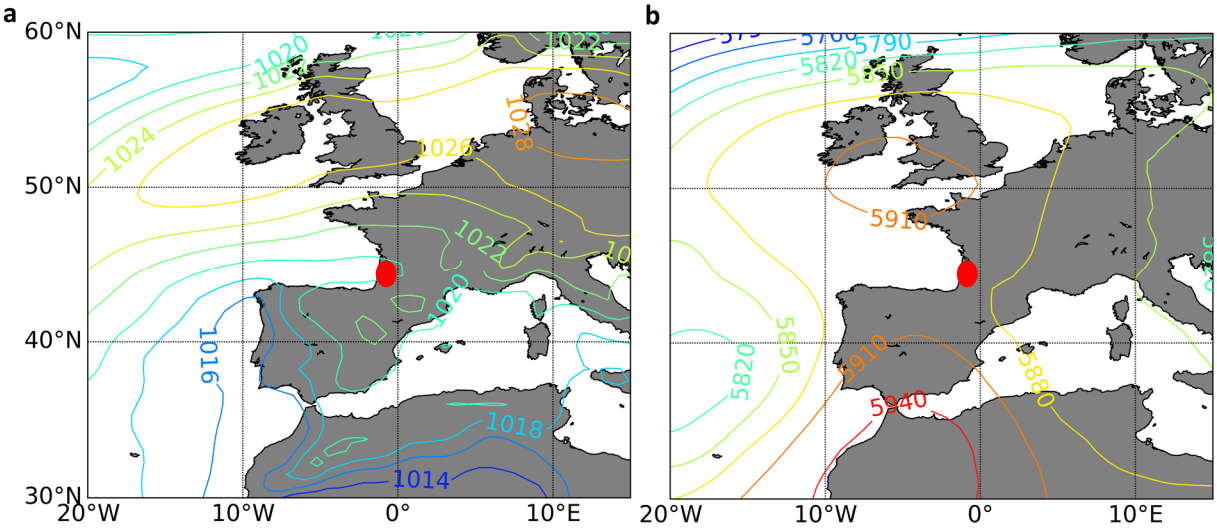

Figure 3: Mean sea level pressure in hPa (left) and geopotential height of the 500 hPa surface in meter with respect to mean sea level (right) for 17 July 2006 at 8 LT. The location of the study region is indicated by the red dot.

is given in section 2.3; see Dee et al., 2011 for a detailed description) shows weak pressure gradients in the study region (Figure 3a). A tongue of high geopotentials is located over a region from Marocco towards Britain (Figure 3b). In the morning at 8 LT (local time), a temperature inversion is present close to the surface, due to longwave cooling that took place during the night. During the day, this inversion was cleared due to strongly positive sensible heat fluxes, while temperatures reached more than 30 °C at 14 LT (Figure 4a). Meteorological stations around the forest reported temperatures above 36 °C that day, which is not visible in the reanalysis data as this data was only available every 6 hours. The specific humidity was highest at the surface, a few hundreds of meters higher up a relatively well mixed layer developed (Figure 4b). Wind speeds were relatively low throughout the atmosphere (Figure 4c). In the morning, the wind was coming from the northeast at the 500 hPa level (± 6km height) , it came from northeast or east at the rest of the levels, except close to the surface and around 9 km height. At the surface the wind was strongly backed and came from the south. Above 3 km height, the wind backed during the day (Figure 4d).

Based on the profiles of 14 and 20 LT, it seems that advection played only a minor role in altering the weather conditions during the day. This can be seen from the relatively small changes in temperature and humidity above the boundary layer (Figure 4a, b). This is deemed important, as it means that local processes are relatively more important than large scale forcings in shaping the weather conditions. This makes this day suitable for the case study. Clouds formed preferentially over the forest (Figure 2b), including deep convection starting in the afternoon. See supplementary material of Teuling et al. (2017) for a time lapse video of the preferential cloud formation. The imposed sensible and latent heat flux from the ERA-Interim data are shown in Figure 4e and f respectively[1]. Both fluxes reach their maximum at 14 LT.

The fraction of the available energy (net radiation minus soil heat flux) that is partitioned to evapotranspiration ranges between 0.57 and 0.86 during the modelled period (see next section), with a mean of 0.64. This indicates (according to the ERA-Interim data) that despite the prevailing heat wave conditions, still a significant amount of soil moisture was available for evapotranspiration.

2.2 Model description

The model we used for our simulations is MicroHH. It consists of a computational fluid dynamics code, solving the conservation equations of mass, momentum, and energy. It is an open source code which allows simulations either using direct numerical simulation or using large eddy simulation (a complete description is available in the model reference paper by van Heerwaarden et al., 2017). The model has been applied in a few studies before (Gentine et al., 2015; van Heerwaarden et al., 2014; van Heerwaarden & Mellado, 2016), more specifically in atmospheric boundary layer studies. The use of this type of models has several advantages compared to the use of observations (adapted from Neggers et al., 2003): Detailed three-dimensional fields of the thermodynamic variables can be simulated, which is very hard to obtain using e.g. aircraft tracks; a very large number of statistics can be produced; and last, the user can control all initial and boundary conditions himself, which helps to elucidate the role of these conditions. This model is appropriate for this study, as it allows for explicitly solving

[1] The imposed fluxes in the model are kinematic fluxes, to obtain them from ERA-Interim we used the initial air density. As the air density varies during the day in the model, this leads to deviations of about 3% between imposed fluxes and fluxes in ERA-Interim

convection and individual clouds while allowing a domain size large enough to obtain output that is statistically valid.

2.3 Model configuration

The model run starts at 8 LT (time zone UTC+2) and ends at 21 LT and thus focuses on convective daytime conditions. The chosen domain extent is 50 km in the x and y-direction. This is rather large knowing that the domain surface is homogeneous, but it is required to obtain model output that is statistically valid. The model will be run in 3D large eddy simulation mode, given the fact that direct numerical simulation would be too computationally expensive for such large model domains. This mode of running the model means that for the finest scales we rely on a so called subgrid model that calculates the correct diffusion and dissipation based on physical laws. A second order Smagorinsky eddy diffusion scheme was used for the subgrid model. For the governing equations, the anelastic approximation was applied. This means that the full Navier Stokes equations are simplified, by making some assumptions that result in the removal of sound waves, while retaining a height dependent reference density (see Bannon [1996] for a derivation).

The vertical extent of the domain is from the surface to 9.5 km height. Reflection of gravity waves at the model top should be prevented. For this purpose, a damping layer was applied from 7.2 km height to the top of the model. Although the onset of cloud formation is mainly a lower level phenomenon, the model extends well above the boundary layer to prevent clouds from entering the damping layer.

The model has a resolution of 94.7 m in the horizontal direction and 23.3 m in the vertical (528*528*408 grid cells). The chosen domain resolution is the result of a trade-off between computational speed and accuracy. Similar resolutions have been used in the past to study shallow cumulus convection, e.g. Siebesma et al. (2003) used a horizontal grid spacing of 100m with a vertical spacing of 40 m, and Brown et al. (2002) employed a horizontal spacing of 66.7m with a vertical spacing of 40 m. The time step was adjusted by the model according to the chosen spatial resolution by setting a maximum tolerable Courant–Friedrichs–Lewy number (Courant et al., [1967] for explanation), equal to 1.2 for all runs.

The initial conditions and surface fluxes for running the model were obtained from the ERA-Interim dataset (Dee et al., 2011) of the European Centre For Medium-Range Weather Forecasts. These data have a horizontal spatial resolution of 0.75°, approximately 80 km (ECMWF, n.d.). Vertically, data is available every 25 hPa from 1000 to 750 hPa, and every 50 hPa from 750 hPa to the top of the model. The temporal resolution of the data is 6 hours (fluxes every 3 hours). The employed variables are temperature, specific humidity, wind and geopotential. The used grid cell from the ERA-Interim dataset is centred on 44.25° N, 0.75° W. The ERA-Interim temperature and specific humidity data compare quite well to the sounding of Bordeaux (44.83° N, 0.68° W) at 14 LT (Figure 4, thin black dashed line). The geostrophic wind is used as large scale forcing, derived from geopotential gradients between the neighbouring grid cells in the ERA-Interim dataset. The initial profiles for the model obtained from the ERA-Interim data are shown in Figure 4 (blue solid line with circles). For the geostrophic wind, small deviations were applied to the ERA-Interim data to smoothen the situation at the surface (Appendix B). Large scale advection is prescribed as a height dependent source/sink term, which is constant in time and in the horizontal direction (Appendix B). This term was roughly estimated by performing a number of model runs with different large scale

source/sink profiles, after which the fit with ERA Interim was compared. Below 2 km height, this term was set to zero for both specific humidity and liquid water potential temperature.

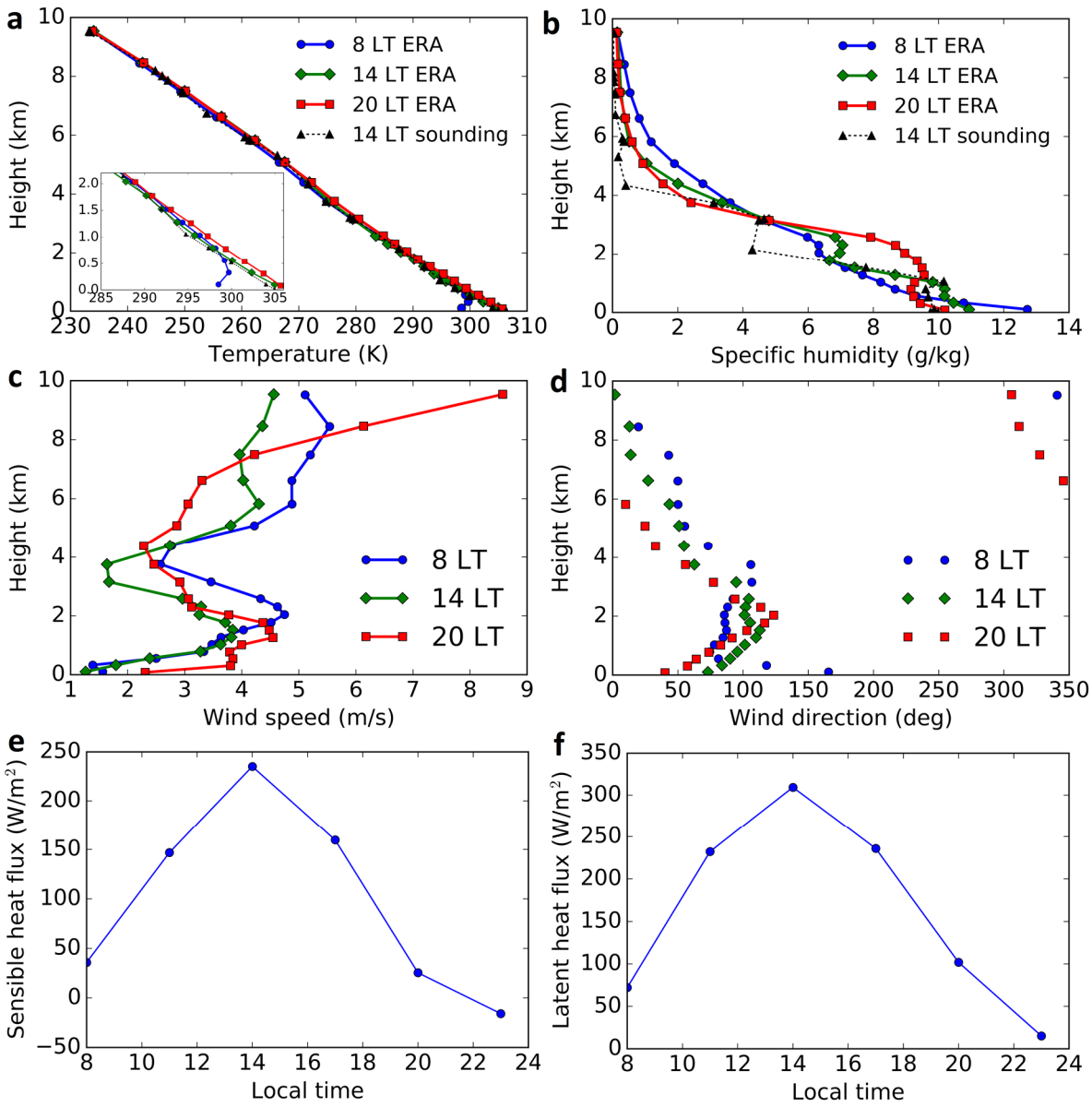

Figure 4: ERA-Interim data for 17 July 2006. (a) shows temperature, (b) specific humidity, (c) the wind speed, (d) the wind direction, (e) the sensible heat flux and (f) the latent heat flux. The 8 LT vertical profiles are used for the model initialisation, the other profiles show the evolution during the day of the variables in the ERA-Interim data. The modelled period spans from 8 to 21 LT, so both surface fluxes in the model are always positive. For temperature and specific humidity, the thin black line shows the vertical profiles obtained from a sounding at 14 LT. All shown heights are relative to the surface (approximately 68m above mean sea level)

The model has no slip ($u, v = 0$) and no penetration ($w = 0$) boundary conditions at the bottom and no penetration and free slip ($\partial u/\partial z = \partial v/\partial z = 0$) boundary conditions at the top. The no slip boundary condition at the bottom is imposed through a model based on Monin–Obukhov similarity theory. The sides have periodic boundary conditions, meaning that what leaves the model at one side enters the model at the opposite side. Random noise is superimposed on the initial temperature and specific humidity fields to provide perturbations that trigger convection. Microphysics schemes were not included in the simulations, to limit the complexity of the cloud formation and to reduce computational load. All model runs were performed on the

Dutch national supercomputer: the Cartesius cluster of the SURFsara Supercomputing Center (www.surfsara.nl). Some more details on the model setup can be found in Appendix C.

2.4 Numerical experiments

A reference run was first performed in which the prescribed surface fluxes are equal to those from the ERA-Interim data[1]. Two main experiments were performed afterwards. The first experiment is called the *Warm* run, in this experiment 5% of the net radiation is added to the sensible heat flux (*H*). In the second experiment, the same amount of energy is added to the latent heat flux (*LE*), this experiment is called the *Wet* run. Net radiation is in this calculation approximated as $H + LE$, meaning that we neglect the soil heat flux. With these experiments, we can investigate the sensitivity of cloud formation to the flux partitioning. As our domain is homogeneous in the horizontal direction, we only look at direct effects of flux partitioning differences. This means we do not include effects of potentially induced mesoscale circulations by a spatial alternation of forest and non-forest surfaces.

One additional experiment was also performed which is only shortly discussed in this study (section 3.3). In this experiment the fraction of energy partitioned to the sensible heat flux was kept constant during the day at 44%. This fraction is close to the maximum possible partitioning to the sensible heat flux during heatwaves according to the data from Teuling et al. (2010). A two moment microphysics scheme (Seifert & Beheng, 2001; with the sedimentation scheme from Stevens, & Seifert, 2008) was turned on in this simulation. The purpose of this experiment was to test the effects of stronger flux partitioning differences between forest and grassland on the convection regime (shallow vs deep).

In our data analysis we sometimes used different realisations of the same run. Those realisations are identical to each other besides for random noise.

2.5 Analysed variables

2.5.1 Liquid water potential temperature

Liquid water potential temperature (θ_l) is defined by Betts (1973) as:

"The potential temperature attained by evaporating all the liquid water in an air parcel through reversible wet adiabatic descent."

In MicroHH it is one of the thermodynamic variables and is calculated as (an approximation by Betts, 1973):

$$\theta_l = \theta - \left(\frac{L_v}{c_p}\frac{\theta}{T}\right) * q_l \qquad (1)$$

Where θ_l is the liquid water potential temperature, θ is the 'normal' potential temperature, q_l is liquid water content (kg kg^{-1}), T is absolute temperature (K), c_p is the specific heat capacity of air at constant pressure and L_v is the latent heat of vaporisation.

2.5.2 Boundary layer height

The top of the planetary boundary layer (PBL) is calculated as the minimum value in the domain averaged vertical profile of the turbulent buoyancy flux (as in Brown et al., 2002). This minimum originates by thermals penetrating in the inversion above the boundary layer, thereby transporting warm air downwards. The quantity is easily obtained from the MicroHH output.

The model calculates the wind velocities and the buoyancy flux (and thus PBL height) at the top and bottom of each grid cell, while the thermodynamic variables are calculated for the middle of each grid cell. Therefore, for the rest of this study, when we talk about thermodynamic variables at the boundary layer top, we actually talk about the thermodynamic variables located half a grid cell (± 11.5 m) below the PBL top.

2.5.3 Condensation inhibition and vertical kinetic energy

Convective inhibition is often used in studies of thunderstorms (e.g. Thompson et al., 2007; Weckwerth, 2000). We slightly adapted the concept for use in our cloud formation study, we call the calculated quantity condensation inhibition, denote it as CIN_{LCL} (J kg^{-1}), and define it as:

$$CIN_{LCL} = -g * \int_{Z}^{LCL} \frac{T_{v,parc}(z) - T_{v,env}(z)}{T_{v,env}(z)} dz \qquad (2)$$

where z is the vertical coordinate, g is the gravitational acceleration, $T_{v,parc}$ and $T_{v,env}$ are the virtual temperatures of the air parcel under consideration and of the environment respectively. The integration borders (and minus sign) distinguish this quantity from the commonly used convective inhibition (CIN). Usually CIN is calculated up to the level of free convection, we only calculate it up to the lifting condensation level (LCL), as we are mainly interested in whether clouds form or not. The CIN_{LCL} quantifies the required energy (per unit mass) an air parcel needs to reach the LCL, starting from a level Z. A negative value means the parcel will net gain energy by ascending. Note that the quantity CIN_{LCL} incorporates both information on temperature (via $T_{v,parc}$) and moisture (via $T_{v,parc}$ and by the height of the LCL) of an air parcel.

We used this concept combined with the vertical kinetic energy (E_k, in J kg^{-1}) of an air parcel to analyse whether air parcels starting from a level Z are able to reach their lifting condensation level (and thus produce clouds). When the vertical kinetic energy of an air parcel is larger than its CIN_{LCL}, the air parcel will be able to reach the LCL. Note that in this we assume that air parcels do not mix with their environment and do not experience friction, so that the buoyancy force is the only force acting on the parcel. When calculating for every cell (air parcel) in a horizontal cross section whether its vertical kinetic energy is larger than the CIN_{LCL}, one can determine the fraction of cells capable of reaching the LCL. Note that in our vertical kinetic energy calculations, all cells with a negative vertical velocity were assigned a value of zero.

3 Results and discussion

3.1 Reference run

This section describes the general evolution of the state of the lower atmosphere in the reference run for the case study of 17 July 2006 and compares the results with the ERA-Interim data.

As a result of a positive sensible heat flux, a mixed layer gradually starts to grow while the temperature at the surface is increasing (Figure 5a). By the end of the day, the near-surface temperature reached 35 °C. The specific humidity (q_t) at the surface is decreasing during the day, despite the positive latent heat fluxes (Figure 5b). This can be explained by the entrainment of dryer air as the boundary layer grows during the day (van Heerwaarden et al., 2009). The boundary layer grows strongly during the day, resulting in heights of more than 2400 m (Figure 5c). The apparent shrinking of the boundary layer in the evening is a consequence of the applied boundary layer top criterion and thus does not have a physical reason. The increasing trend in the upper air temperature and the decreasing upper air moisture is a result of the prescribed

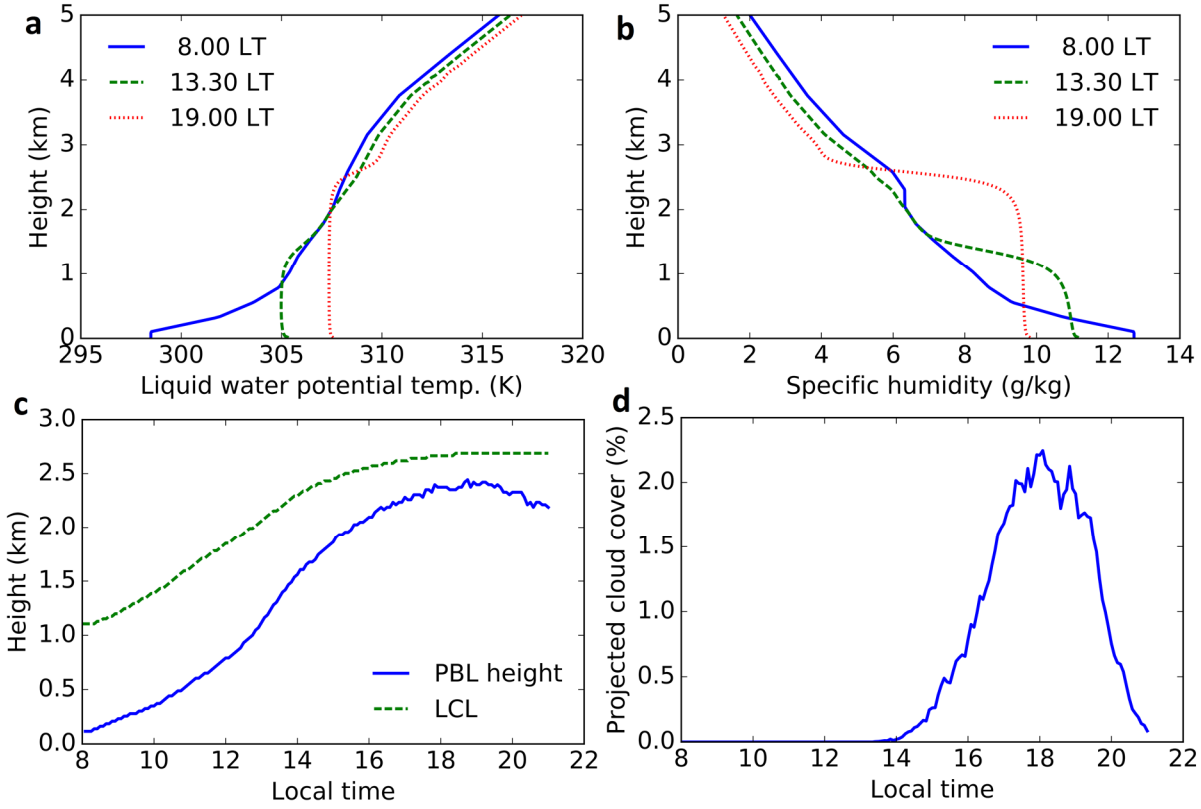

Figure 5: Evolution of the liquid water potential temperature (a) and the specific humidity (vapour + liquid) (b). (c) shows the evolution of the boundary layer and lifting condensation level heights, (d) shows the cloud cover. The cloud cover takes clouds at all heights into account by projecting them on the surface. The vertical height axis in (a), (b) and (c) shows height above the model surface. All quantities are for the reference run and are averaged over the horizontal extent of the domain.

large scale forcings. These forcings represent large scale advection (see Methodology). Clouds (cumulus) started to form around 13.30 LT, the cloud cover reached a maximum value of a little more than 2% at 18 LT (Figure 5d), whereafter it decreased rapidly due to decreased surface fluxes. Around the time of maximum cloud cover, the planetary boundary layer (PBL) height is still lower than the lifting condensation level (LCL, calculated based on a surface air parcel), but the difference is approximately at its lowest (Figure 5c). As the plots show the areal

averaged variables, locally some rising plumes will reach altitudes higher than the LCL, explaining the formation of clouds. The convection is shallow, as the top of the highest clouds does not surpass 3500 m (not shown). The cloud base increases in height from approximately 1500 m at the onset of cloud formation to approximately 2400 m at the end of the day (not shown). This increase is caused by the warming and drying of the PBL due to the PBL growth and surface heating during the day (Figure 5a, b).

The differences between the model results and the ERA-Interim data (Figure 6) are below 2 K and 1.50 g kg^{-1} throughout the domain for θ_l and q_t respectively. Despite this generally speaking good match, at the end of the day liquid water potential temperature (θ_l) is overestimated close to the surface. This may be due to some advection near the surface, or because no radiative cooling is present in the model. The root mean square error[2] (below 4.5 km) at 14 and 20 LT for θ_l amounts to 0.7 and 1.0 K respectively. For the specific humidity at 14 and 20 LT it amounts to 0.8 and 0.5 g kg^{-1} respectively, quantifying the good match visible in Figure 6. When taking the full domain into account, the root mean square error is even lower. Note that the model does not show deep convection in the reference run (Figure 6d), although it was visible in the satellite image (Figure 2). This discrepancy can be caused by several reasons, this is discussed in section 3.3. The next section will investigate the sensitivity of cloud formation to the sensible and latent heat fluxes.

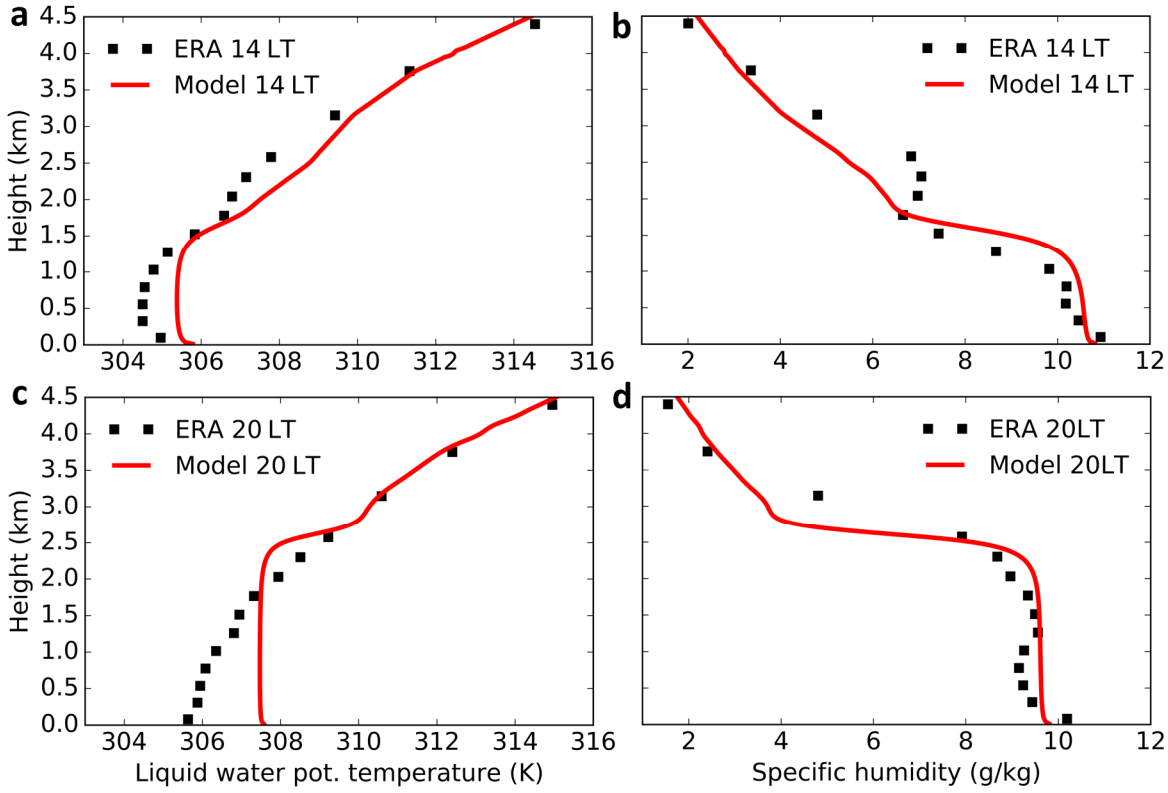

Figure 6: Comparison between the model results (red lines) and the ERA-Interim data (black dots) for liquid water potential temperature (a, c) and specific humidity (b, d) for two different times. Only the lower part of the domain is shown, as this is the part where cloud formation takes place. Specific humidity encompasses both water vapour and liquid water. Heights are relative to the model surface (approximately 68m above mean sea level).

[2] The root mean square error was calculated by interpolating the model data to the ERA-Interim heights. No weighting was applied, meaning that all data points were given equal importance.

3.2 Flux partitioning experiments

In the experiments presented below, the surface fluxes were altered by adding 5% of the sum of the latent and sensible heat flux (which together approximate the net radiation) to either the sensible or latent heat flux. In the *Warm* experiment, this amount was added to the sensible heat flux, while in *Wet* it was added to the latent heat flux.

As expected, both the *Warm* and *Wet* runs show an increase in cloud cover compared to the reference run due to an extra input of energy (Figure 7a). However, the effect of adding an extra amount of energy was clearly larger when the energy was added to the sensible heat flux compared to when it was added to the latent heat flux. In *Warm*, the maximum cloud cover amounts to 3.9%, while this is only 2.9% in *Wet*. Additionally, during the period from 14 LT to the end of the simulation period, the mean cloud cover amounts to 2.0% for *Warm* while it was only 1.4% in *Wet*. The differences are not only visible in the cloud cover, but even more in the liquid water path. Differences almost as large as a factor of 2 occur between the runs (Figure 7b). The following sections are mainly devoted to the explanation of these results.

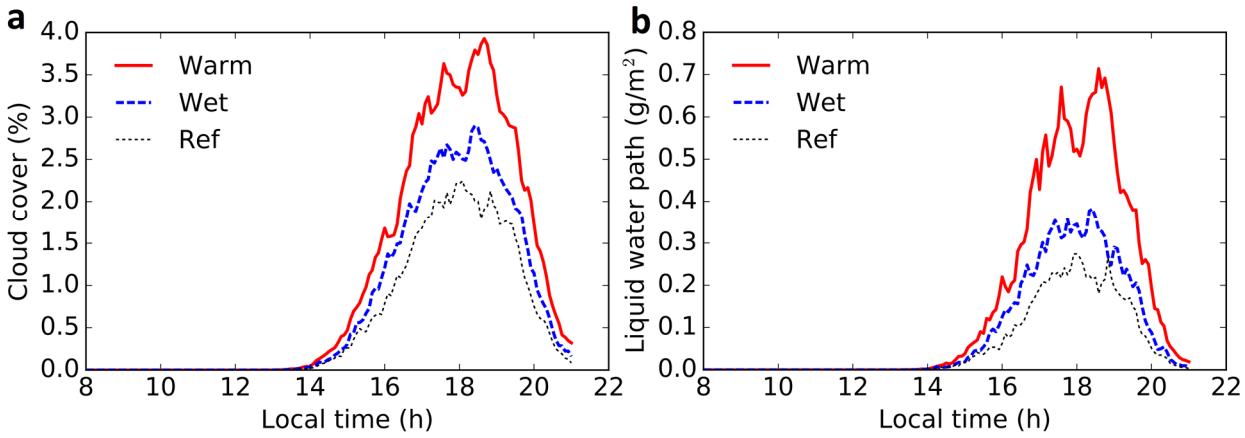

Figure 7: Cloud cover (a) and liquid water path (b) for the *Warm*, *Wet* and reference (*Ref*) runs. Cloud cover is calculated by projecting all clouds on the surface. Both quantities are averaged over the domain.

3.2.1 Mean quantities and frequency distributions

To explain these results, we first look at the difference between the LCL and the PBL height. If the LCL is located too far above the PBL top, thermals penetrating the PBL top will not reach the lifting condensation level as they would need to travel a long distance through the inversion layer. This quantity was used by e.g. Vilà-Guerau de Arellano et al. (2012) as a metric and proxy for boundary layer cloud formation. The run with the larger sensible heat flux (*Warm*) has a larger domain mean PBL height (Figure 8a), due to the warmer and more vigorous thermals. However, the domain mean lifting condensation level (not shown) is also increased due to an increased amount of entrained dry air and a smaller evapotranspiration. These effects seem to be largely compensating each other, resulting in small differences in the quantity PBL height minus LCL between both runs (Figure 8b). As both the LCL and the height reached by the thermals (PBL height) vary horizontally (Wilde et al., 1985), the mean difference does not necessarily quantify the full potential for cloud formation.

Another measure that is often used to quantify the potential for cloud formation is the relative humidity (RH) at the PBL top (e.g. Ek & Mahrt, 1994; Ek & Holtslag, 2004; van Heerwaarden & Vilà-Guerau de Arellano, 2008; Gentine et al., 2013). The time series of RH at the boundary layer top is shown in Figure 8c, it was calculated here as the horizontal mean vapour specific

humidity (q_v, where subscript v means vapour) at the PBL top divided by the horizontal mean saturation specific humidity (q_s) at the PBL top. Only during the first hours of cloud formation the mean relative humidity seems to be a bit higher in the *Warm* run, by 17 LT the differences are almost zero. During the last simulation hour RH is even lower in *Warm* compared to *Wet*. Additionally, cloud formation is taking place at extremely low values of RH, even at values below 60%. As a comparison, the simple cloud cover parameterisation scheme used by Benjamin and Carlson (1986) starts cloud formation only at 75% mean RH. It is also remarkable that the cloud cover starts to decrease earlier in the evening compared to the mean RH (Figure 7a vs Figure 8c). This quantity can thus not explain the enhanced cloud cover for the *Warm* run in this study. There are three reasons why this might be the case:

A first source of error is that when calculating the mean RH, the calculated quantity $mean(q_v) / mean(q_s)$ is not necessarily equal to the mean of $q_v / q_{s,}$, especially in the presence of a correlation between those quantities. There indeed appears to be a correlation between q_v and q_s at the boundary layer top (Figure 8d). In case of cloudy cells, there is a positive correlation, in case of non-cloudy cells there is a negative correlation. We can understand these correlations as follows: the saturation specific humidity at a specific height is mainly a function of temperature (T), as pressure fluctuations are rather small. A correlation between q_t and q_s thus also means a correlation between q_t and T. As the mixed layer is both warming and drying during the day (Figure 5a, b), the negative correlation is caused by the entrainment of air from above the PBL, with a high θ_l and a low q_t. This air mixes with the air that was already present in the PBL. The positive correlation for the cloudy cells is caused by the release of latent heat of condensation, which increases the temperature. The positive correlation for the cloudy cells will barely influence the calculation of the mean RH, as for cloudy cells the RH is always very close to 100%. For the non-cloudy cells, the negative correlation will influence the result as follows: Very small and very large values of q_v lead to even extremer values in RH due to the correlation. This will increase the weights of these cells when calculating the mean RH as the mean of all RH values. When calculating the mean RH as the mean of q_v divided by the mean of q_s, this effect is not taken into account, potentially leading to errors. A mathematical explanation of this error is given in Appendix E.

Besides the correlation, another reason for differences between the mean of (q_v / q_s) and the quantity $mean(q_v) / mean(q_s)$ arises when the q_s deviations from the mean are not negligible compared to the mean q_s (Appendix E). Furthermore, we should note that q_s is a strongly non-linear function of temperature. This means that errors might also arise in the calculation of the mean q_s when calculating it based on the mean temperature. In this study, the error introduced by the reasons explained in this and the previous paragraphs seems to be well below 1% however.

A second and (for this study) more important point to consider is that the mean RH does not directly provide information on what fraction of the horizontal area that is saturated. In larger scale models, this information (subgrid-scale) cannot directly be obtained. One way to deal with this is to parameterise the probability density function (pdf) of total specific humidity, after which the cloudy fraction can be determined by integrating the saturated part of the pdf (Tompkins, 2002). Preferably, variations in q_s and the correlation between q_s and q_t should be taken into account as well (Figure 8d). As we are using LES however, we were able to directly calculate relative humidity for each cell in a horizontal cross section at the level of the boundary layer top. From this we calculated the probability distribution function of RH to check whether

there are more cells with high values of relative humidity in the *Warm* run. What is remarkable in these pdf's is the presence of two peaks (Figure 9a). We postulate that the size and location of the peak at high relative humidity is more relevant for cloud formation than the mean of the

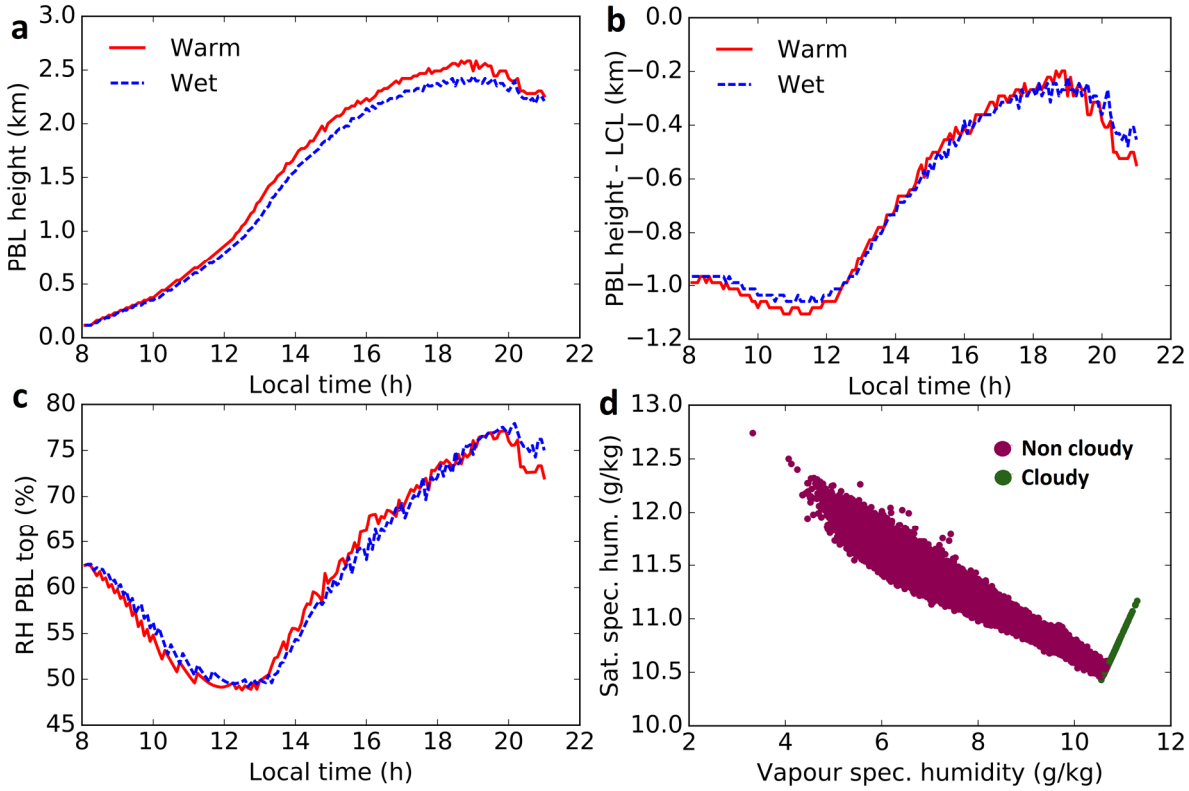

Figure 8: Domain mean boundary layer height (a), domain mean boundary layer height minus domain mean LCL (b) for the *Warm* (red) and *Wet* (blue) runs. In (c) the mean RH time series at the PBL top is shown. (d) Shows a scatterplot of total specific humidity (q_t) and the saturation specific humidity (q_s) for the *Warm* run at the boundary layer top at 18 LT. The green and purple dots are for cloudy (liquid water content > 0) and non-cloudy cells respectively.

whole distribution. At 18 LT, the approximate peak time of cloud cover, there are more cells with high relative humidity in the *Warm* run (Figure 9a). However, when looking at a longer period, it seems that there are still more cells with a higher RH in the *Warm* run, but the differences are smaller between the runs (Figure 9c, d). We also calculated for both runs the range of probability densities for each RH bin that were attained during the main period of cloud formation (shaded areas in Figure 9d). This range was (just as the peak at high RH) shifted to the right for the *Warm* run. Those differences between the runs will have an impact on the cloud formation, but they are unlikely to explain the rather large differences in cloud cover between the runs.

The total and saturated specific humidity distributions also have two peaks (not shown). This shows that the pdf's of these quantities are complex to parameterise (as might be done in large scale models), the assumption of a Gaussian q_t distribution (as e.g. done by Sommeria & Deardorff, 1977) seems to be invalid for the LES data in this case study.

In case of mixed layer models the probability density functions cannot be obtained explicitly and thus the mean RH is often the only information (explicitly) available. The results of this study show that the use of the mean PBL top RH based on mixed layer models is insufficient as an indicator for cloud formation for this case study.

The third reason is that RH at the PBL top is not necessarily a complete surrogate for cloud formation. In this study, the location of the maximum cloud fraction is higher than the boundary layer top. This might partly be explained by the horizontal spreading of air parcels, but it is also important to realise that cloud formation might still be enhanced even when the RH of air parcels of both runs is identical when reaching the PBL top. This might be caused by differences in how much resistance air parcels experience in the region between the PBL top and the lifting condensation level. Section 3.2.3 will elaborate on this.

Whether sensible or latent heating favours a higher relative humidity at the PBL top depends on atmospheric variables such as the free tropospheric temperature and its lapse rate, the relative humidity above the boundary layer (Gentine et al., 2013) and the large scale vertical velocity (Ek & Mahrt, 1994). Figure 5 of Gentine et al (2013) shows (depending on atmospheric variables) whether an increased partitioning to the latent or to the sensible heat flux would enhance the RH at the PBL top. From our model data (*Wet* run) around solar noon (free tropospheric RH estimated as 50%, free tropospheric pot. temp. = 29 °C, fraction of energy partitioned to LE = 0.59, pot. temp. lapse rate = 2.8 K km^{-1}) we can roughly estimate that in this figure, our case would be located in the negative sensitivity region (sensitivity of RH at PBL top to an increase in the fraction of energy partitioned to *LE)*. This means that the mean RH at the PBL top should be higher in the *Warm* compared to the *Wet* experiment. This is not wat we observe in our model simulations (we observe similar RH), although we do see a higher cloud cover in the *Warm* run. We should however mention that there is a very large uncertainty in estimating the parameters based on the LES data. The available energy is also slightly larger in our data (+ 11%) compared to the value used for constructing figure 5 in Gentine et al. (2013). Furthermore, the applied fraction of energy varies during the day in our simulations, while it is constant in Gentine et al. (2013).

3.2.2 Rising air plumes

A feature that deserves more explanation is the presence of two peaks in the RH distribution at the PBL top. It turned out that the two different types of air parcels could easily be separated on the basis of buoyancy (Figure 9b, d). The cells with the highest relative humidity are the least buoyant cells. At first sight this may seem like a surprising result, as wet plumes originating at the surface become buoyant and rise towards the PBL top. Once they arrive near the PBL top however, they will become colder than their environment due to the presence of an inversion in θ_l, explaining their lower buoyancy compared to the environmental air at the same level (Couvreux et al., 2010; Lenschow & Stephens, 1980). This explains why two different types of air parcels can be found at the PBL top.

When separating between plumes and non-plumes, it is clear that most of the somewhat thicker clouds form above the rising plumes (Figure 10a). The plumes also seem to contain stronger vertical velocities than the non-plumes (Figure 10b). When separating the plumes on the basis of specific humidity, this is more clearly visible (Appendix D, Figure D1). The plumes also contain negative vertical velocities, this can be explained by the fact that some of the air parcels belonging to the plumes who end up in the inversion layer (and are negatively buoyant) will eventually return towards the PBL (Lenschow & Stephens, 1980). Another reason for the presence of negative vertical velocities is the presence of small scale turbulence within the plumes (Williams and Hacker, 1992). To get more insight into the physical processes, we also made scatterplots of the thermodynamic variables at the PBL top. There is a clear negative correlation between q_t and θ_l (Figure 10c), caused by entrainment of air, as was explained in

section 3.2.1. This negative correlation was also found during the BOMEX measurement campaign (fig. 1 of Neggers et al., 2002). Furthermore, it seems that strongly positive vertical velocities only occur for a narrow range of q_t and θ_l values (Figure 10c, d). This narrow range can be explained by the fact that only air parcels which are heated at the surface can attain sufficient buoyancy to acquire high vertical velocities. The mean value of q_t and θ_l at the surface lies at the dry and warm end of this range (Figure 10c, black square). As the PBL is drying and warming during the day (Figure 5a, b), by the time the air parcels reach the PBL top, the mean surface quantities will have slightly changed. This can explain why the mean value of q_t and θ_l at the surface lies at the dry and warm end of the range. Possibly other factors play a role in this as well.

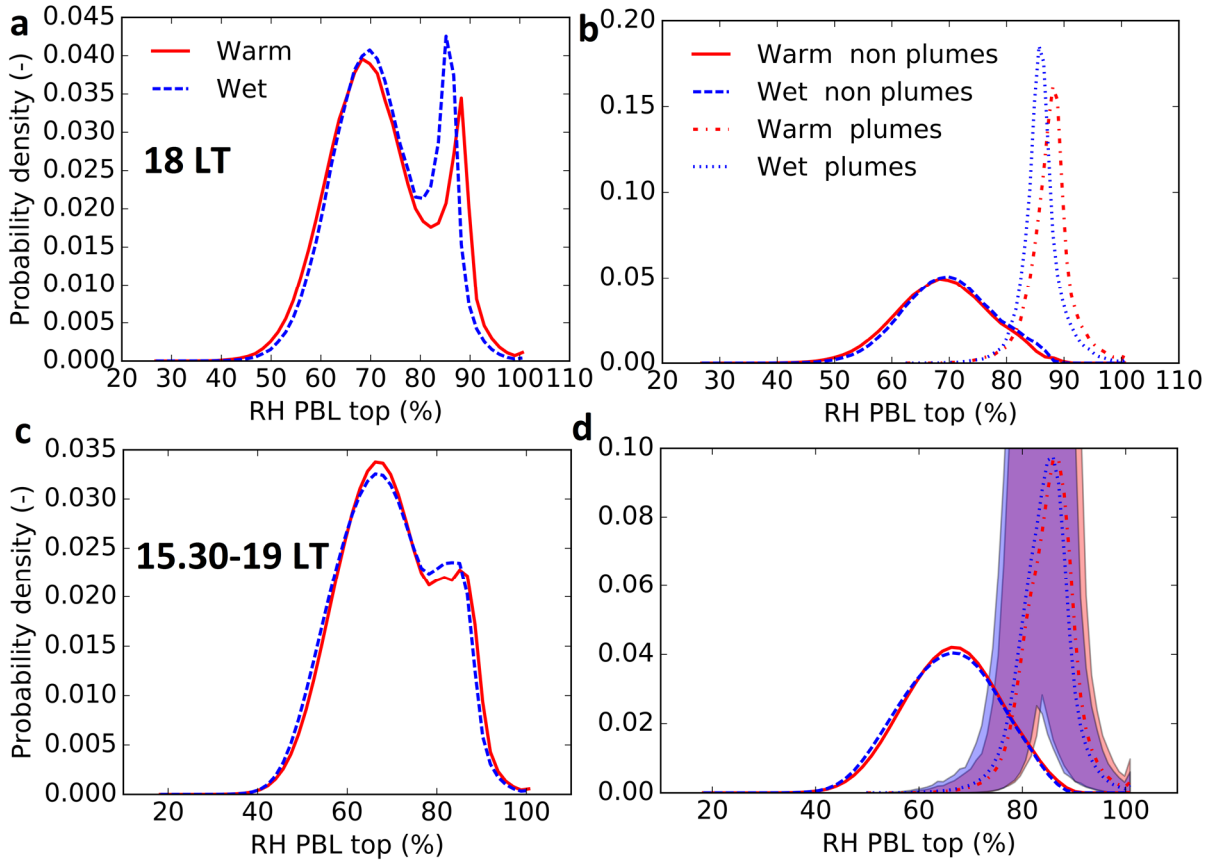

Figure 9: Relative humidity at the PBL top at 18 LT for both runs (a), conditionally sampled in (b) using buoyancy as criterion. The 20% least buoyant cells are defined as plumes, separate probability density functions are made for plumes and non-plumes. (c) shows the same as (a), but for the period 15.30-19 LT, (d) shows the same as (b), but for the period 15.30-19 LT. In (d), the shaded blue (red) area indicates for each bin of the plumes the maximum and minimum probability density that was reached during the period 15.30-19 LT for the *Warm* (*Wet*) run. Fifty bins were used for the probability density functions.

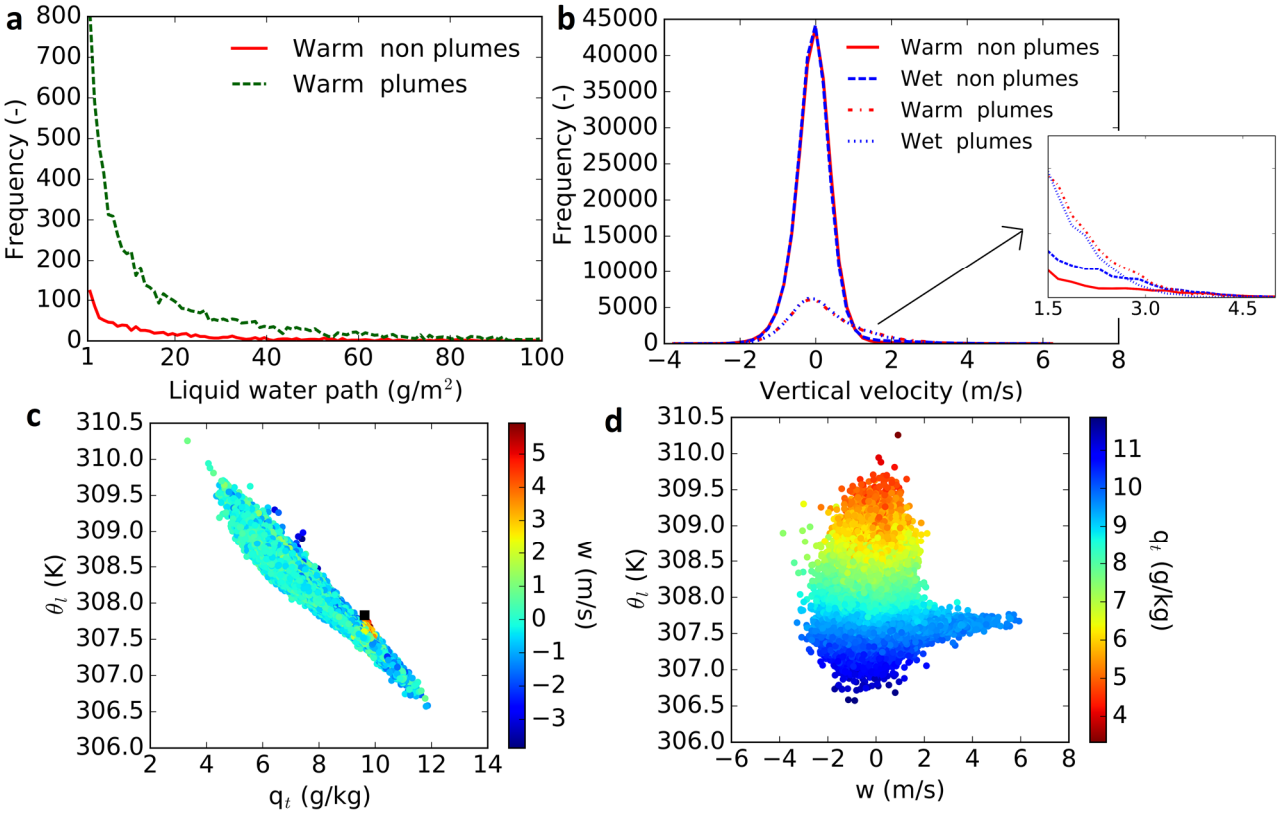

Figure 10: Frequency distribution of liquid water path (a), conditionally sampled as in Figure 9. Note that only the larger values of liquid water path are shown. (b) shows the frequency distribution of the vertical velocity (w), with the inset picture focusing on the larger values of w. In (c) the correlation between θ_l and q_t is shown, with the vertical velocity as colour scale. The black square shows the domain averaged values near the surface. In (d) the correlation between θ_l and vertical velocity (w) is shown, using q_t as colour scale. All plots are obtained at 18 LT, at the boundary layer top, and belong to the *Warm* run ((b) shows both *Warm* and *Wet*). Fifty bins were used for the histograms (for the full data range).

3.2.3 Condensation inhibition

The boundary layer is expected to be more vigorous for the *Warm* run as the stronger sensible heat flux can lead to larger vertical density differences within the PBL and thus stronger vertical motions. The boundary layer is also warmer in this run. To quantify what effect these properties have on cloud formation, we selected a horizontal cross section and determined for both runs the number of cells that were in theory capable of reaching the lifting condensation level starting from this cross section. For this we analysed the condensation inhibition (CIN_{LCL}), see section 2.5 for the applied formula. It quantifies the energy required to reach the LCL for an undiluted parcel ascent from a level Z up to the lifting condensation level. We also calculated the amount of vertical kinetic energy the parcels had at the start of their ascent. When the kinetic energy (E_k) is larger than the CIN_{LCL}, the parcel is able to reach the LCL.

The number of cells capable of reaching the LCL from a horizontal cross section at 2000 m height[3] is more than twice as high for the *Warm* run (Table 1). It appears that this is mainly caused by a lower value of the CIN_{LCL}, despite the higher LCL in the *Warm* run.

[3] Regarding the cross section at 2000 m: for the thermodynamic variables, the cross section was taken at 1991 m, for the vertical velocity (w) it was taken at 2002 m. Regarding the cross section at 500 m: for the thermodynamic variables, the cross section was taken at 501 m, for w it was taken at 489 m. The differences in height for w and the thermodynamic variables are due to differences in heights were the model calculates these variables.

The mean vertical kinetic energy is also slightly larger for *Warm*. We tested the effect of this by subtracting the mean vertical kinetic energy difference (for cells with $E_k > 0$) between both runs from the kinetic energy in *Warm*. This led only to a reduction of 0.2% in the fraction of cells capable of reaching the LCL from the 2000 m level. We also assigned the mean kinetic energy of the 3% most energetic cells of the *Warm* run to all cells of both the *Warm* and the *Wet* run. In this experiment, the fraction of cells reaching the LCL was still more than a factor of 2 higher in the *Warm* run. This suggests that kinetic energy differences play a small role compared to CIN_{LCL} differences.

Table 1 also shows that the average air parcel is in both runs by far not capable of reaching the LCL. Therefore it is important to not just look at mean quantities, but to consider the probability density distributions of CIN_{LCL} and E_k (Figure 13). Clearly, the distributions are more favourable for cloud formation in the *Warm* run, as the number of high E_k and low CIN_{LCL} cells is higher in this run. The number of cells capable of reaching the LCL is (for both runs) enhanced by the presence of a negative correlation between CIN_{LCL} and E_k (Appendix D, Figure D2), such that the most energetic parcels experience the least resistance for reaching the LCL. For the cross section at 500 m height[3] the fraction of cells theoretically capable of reaching the LCL is about an order of magnitude higher than at 2000 m (Table 1), this can be explained by mixing as in reality many parcels do not rise undiluted from the surface to the PBL top (Williams & Hacker, 1992). The number of cells actually capable of reaching the LCL will in reality thus be lower. However, we believe our conclusions from the undiluted parcel theory will qualitatively not change in the presence of mixing, as the differences (in % of cells $E_k > CIN_{LCL}$) between the runs only seem to increase with height (Table 1).

As an alternative way of analysing the situation, we also calculated the vertical distance air parcels could travel before being stopped by the buoyancy force (Figure 11a, b). Some cells are capable of rising more than one km, more than sufficient to reach their LCL. As expected, the largest travel distances are found in the *Warm* run. We furthermore analysed the relation between the distance the air parcels can travel and the initial vertical velocity they had when starting their ascent from 2000 m height. Apparently, the vertical velocity is the main factor which determines how far air parcels can travel (Figure 11c, d). At first sight, this may seem contradictory to the theory presented above. However, the vertical velocity differences between both runs are rather small, therefore the influence of vertical velocity differences on the travel distances is small. The presence of two types of air (section 3.2.1) is also visible in these correlation plots. The relatively wet air parcels are the ones with a high vertical velocity. This indicates that these cells belong to the rising plumes, as the surface is the only moisture source.

To explain why CIN_{LCL} is lower in the *Warm* run, we analyse the virtual potential temperature (θ_v) profiles of both runs (Figure 12). Air parcels rising from the surface become negatively buoyant slightly above the PBL top (assuming no mixing for ease of explanation). Although the LCL is higher in the *Warm* run, the PBL top is higher as well (see also Figure 8b), leading to small differences in the vertical distance air parcels have to travel through a region in which they are negatively buoyant. We can however see that the profile in the boundary layer is more or less shifted to the right in the *Warm* run compared to the *Wet* run. This is due to the enhanced surface heating and entrainment in the *Warm* run. This means that in *Warm*, the parcels (which are warmer than in *Wet*) will be less negatively buoyant when they enter the layer between the PBL top and the LCL, explaining part of the lower CIN_{LCL}.

Table 1: Columns from left to right: Mean lifting condensation level (LCL) for both runs; mean vertical kinetic energy (E_k); mean energy required to reach the LCL; percentage of all the cells in the cross section at 2000 m which can reach the LCL; percentage of all the cells in the cross section at 500 m which can reach the LCL. The value of E_k shown in the table is only for the cells with a positive vertical velocity. In the calculations in the last two columns, the LCL is calculated separately for every cell. The calculated quantities in the first four columns belong to the cross section at 2000 m. All quantities are for 18 LT. The calculation method assumes undiluted ascent of parcels.

	LCL (m)	**E_k (J/kg)**	**CIN_{LCL} (J/kg)**	**% cells E_k > CIN_{LCL} at 2000 m**	**% cells E_k > CIN_{LCL} at 500 m**
Warm	2812	0.99	6.88	2.7	21
Wet	2714	0.76	8.76	1.2	17

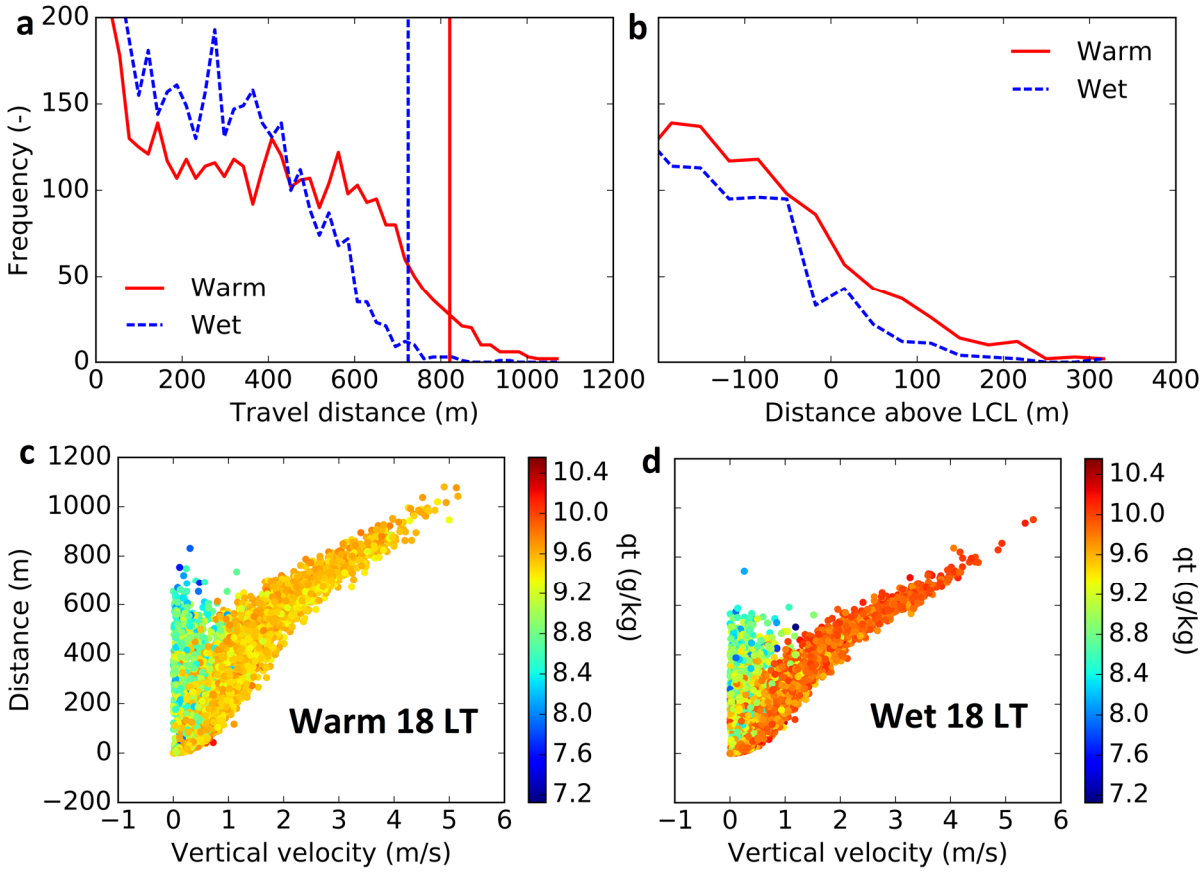

Figure 11: Frequency of travel distance of undiluted parcels starting at a horizontal cross section at approximately 2000 m at 18 LT, calculated with a simple parcel model (a). The resulting frequency of travel distance above the LCL is shown in (b). In (a), the vertical red and blue lines indicate the distance required to reach the mean LCL for the *Warm* and *Wet* runs respectively. In (b) the LCL is calculated for every cell separately. Note that in (a), a travel distance of zero occurred the most frequently, the vertical axis does not display this large frequency for clarity of the figure. Similarly, b only shows a subset of the data, the part where travel distances are closest to the LCL. (c) and (d) show the correlation between the vertical velocity and the travel distance for the *Warm* and *Wet* run respectively. The colours indicate the specific humidity of the parcels. Negative vertical velocities were set to zero. For computational efficiency, only every 5th cell in the data was sampled. The travel distances are calculated taking the buoyancy force and the initial vertical kinetic energy of the parcels into account. Fifty bins were used for the histograms (for the full data range).

Furthermore, the profile in the region between the PBL top and the LCL seems to be shifted to the left in the *Warm* run (Figure 12a). An experiment was done in which the environmental profile above the boundary layer top in the *Warm* run was replaced with the profile of the Wet run. This decreased the fraction of cells capable of reaching the LCL from 2.7 to 1.5%, showing it is an important factor. The shift of the θ_v profile to the left above the PBL is partly the effect of the cloud formation itself, as before the onset of cloud formation this shift seems to be very

limited (Figure 12b). The thermals and clouds reaching altitudes higher than the PBL top bring in colder and moister air to the inversion region, explaining the decrease in θ_v in this region. It is however somewhat difficult to disentangle cause and effect in this: The reason thermals bring in more cold and moist air in the inversion region might be caused by the lower CIN_{LCL} itself. Via the mechanisms described above, the clouds (and thermals) make it easier for subsequent clouds to form. Chaboureau et al (2004) also reported a positive effect of clouds on subsequent cloud formation, in their study moistening by the formation of cumulus clouds triggered the transition from shallow to deep convection.

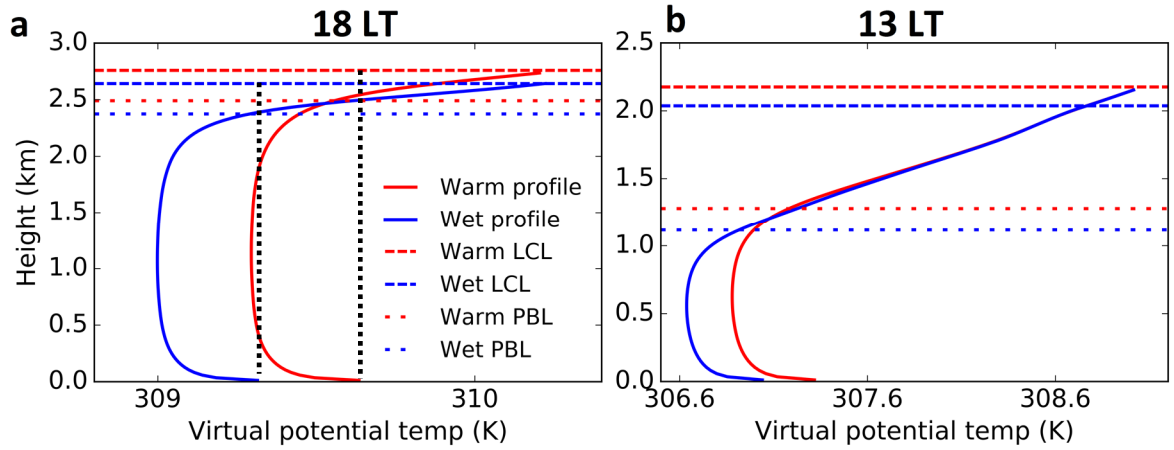

Figure 12: Vertical profile of virtual potential temperature for the *Warm* (red) and *Wet* (blue) runs at 18 LT (a) and 13 LT (b). The lowest (dotted) horizontal line for each run is the PBL top, the upper (dashed) horizontal line is the LCL. The black dotted lines show air parcels rising from the surface without mixing for both runs.

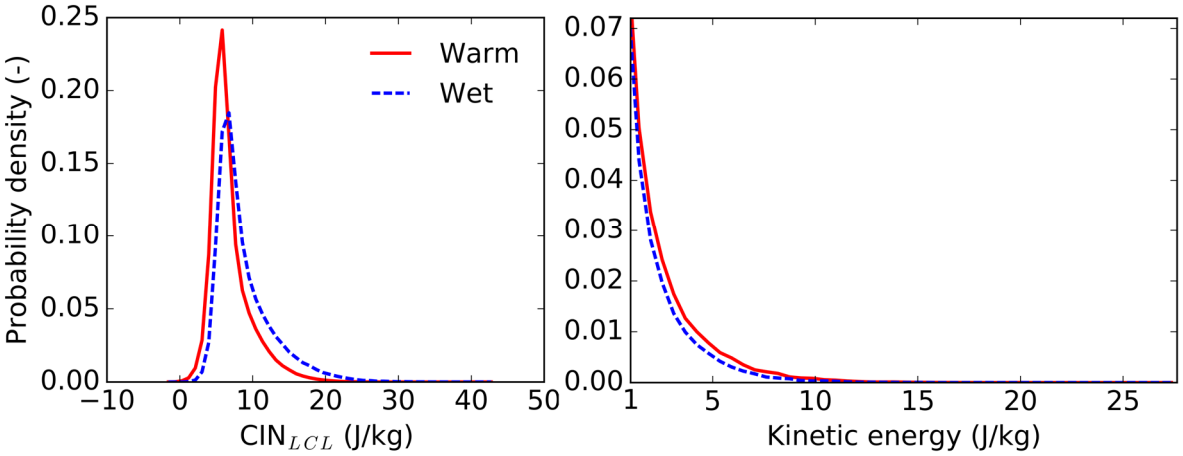

Figure 13: Probability density functions of CIN_{LCL} and vertical kinetic energy (E_k) for a cross section at 2000 m at 18 LT. The E_k distribution only shows values larger than 1 J kg^{-1}. Fifty bins were used (for the full data range).

Another difference which contributes to the lower CIN_{LCL} is the maximum buoyancy an air parcel rising from the surface can attain. This is visible in Figure 12 as the difference in θ_v between the surface and the minimum in the vertical profile. This difference is 0.02 K larger in the *Warm* run. This has the consequence that air parcels released from the surface in the *Warm* run will become negatively buoyant at a slightly greater height above the PBL top compared to *Wet*, thereby decreasing the region in which they experience a negative buoyancy. To test the importance of this factor, we slightly increased θ_v of the parcels in the *Wet* run, such that the maximum buoyancy of parcels based on the mean properties becomes identical

for both runs. This only increased the fraction of cells capable of reaching the LCL by 0.2%, which means this factor is of minor importance.

We also analysed whether there was a larger number of cells with strong positive θ_v deviations (θ_v minus the horizontal mean of θ_v) in the *Warm* run. As the relation between θ_v of the air parcels and the CIN_{LCL} is strongly non-linear, differences in the θ_v distribution might also contribute to the explanation of the lower mean CIN_{LCL} in the *Warm* run. Those differences between the runs seem to be limited however (Appendix D, Figure D3).

3.3 Flux partitioning contribution to enhanced forest cloud cover in our case study

We have shown that for this case, an increase in the sensible heat flux leads to stronger cloud formation than an increase in the latent heat flux. Keeping in mind that forests in this region do have a higher sensible heat flux (Teuling et al., 2010), we showed a possible mechanism for the observed enhanced cloud formation.

However, from satellite images (Figure 2) it is clear that deep convection was present on that day, while our simulations only showed shallow convection. What is interesting to note is that our simulations do show the potential for deep convection, once air parcels pass the level of free convection (LFC), there is a large region in which they are positively buoyant (Figure 14). It seems however that relatively few parcels are passing the LFC, and those who do are apparently diluted by mixing rather quickly, causing them to lose their buoyancy. This is related to the fact that the generated clouds are rather small, small clouds entrain relatively more than deep clouds (Khairoutdinov & Randall, 2006; Rieck et al., 2014), causing them to dilute faster. Possibly, the formation of a forest breeze (e.g. Wang et al., 2009; Gambill & Mecikalski, 2011) or frictional convergence come into play here, providing an extra lifting mechanism that leads to deep convection. Another possibility is that some synoptic forcing, e.g. a sea breeze, triggered the deep convection. These types of phenomena are not necessarily present in the ERA-Interim reanalysis data, as e.g. the scale of a sea breeze can be smaller than the grid size of ERA-Interim (Abbs & Physick, 1992).

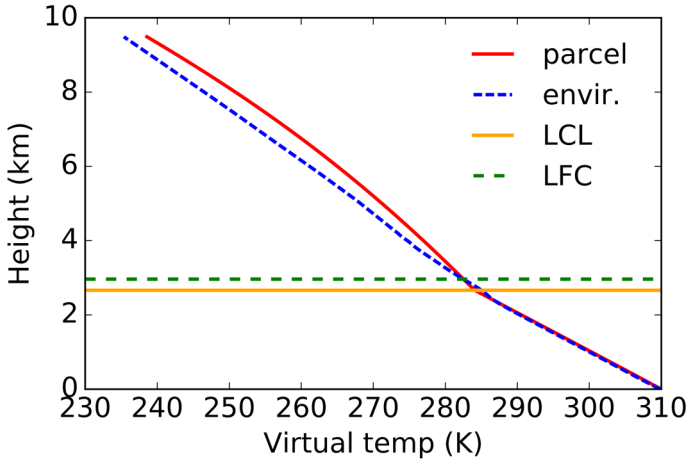

Figure 14: Virtual temperature profile for the reference run (blue dashed line), virtual temperature of an undiluted air parcel rising from the surface (red solid line), level of free convection (green dashed horizontal line) and lifting condensation level (orange solid horizontal line). The situation for 18 LT is shown.

One experiment was also performed in which flux partitioning differences were a little stronger (44% of net radiation partitioned to *H* during the whole day) and close to the maximum possible differences during heatwaves according to the data from Teuling et al. (2010). A two moment microphysics scheme was also turned on to include possible effects of evaporating rain and associated cold pools (e.g. Khairoutdinov & Randall, 2006). The model run produced slightly higher clouds and a higher cloud cover in the evening, but a transition to deep convection was not observed. This suggests that flux partitioning differences alone cannot be the reason for the preferential deep convection over the forest.

Another interesting feature apparent in our simulations is that the (surface based) convective available potential energy (see Blanchard [1998] for explanation and the applied formula) is higher for the *Wet* than for the *Warm* run (Appendix D, Figure D4). This suggests that even though it is harder to form clouds, they would more easily grow deep in the *Wet* run. This argues that the main reason for the preferential deep convection over the forest in this case study is likely to be found in the deep convection triggering mechanism. Additional experiments are needed to pinpoint the exact reason for the absence of deep convection.

3.4 Generalisation of results

Whether an increase in sensible or latent heating will lead to enhanced cloud cover is strongly dependent on atmospheric conditions such as the thermal stability (Huang & Margulis, 2011). In case of a weak thermal stability an increase in the sensible heat flux seems to increase the cloud cover (Ek & Holtslag, 2004; Huang & Margulis, 2011). As stability is variable in time and (on larger scales) also in space, preferential cloud formation (via flux partitioning differences) over the forest will also be space and time dependent. If cloud cover differences induced by differences in flux partitioning play an important role in the observed higher forest summer cloud cover in the study of Teuling et al. (2017), it means that for a significant part of the time, thermal stability should be low in the region.

Not all forests do have a higher sensible heat flux than their surroundings. As an example, in the Amazon, during the dry season sensible heat fluxes are higher over pasture than over forest (Fisch et al., 2004), contrary to the situation in our case study. The results of this case study should therefore be extrapolated to other forest areas with caution, as the surface conditions might be different.

4 Conclusions

We have analysed how flux partitioning differences affect cloud formation over forests. A case study was performed for the forest of Les Landes (France). We selected a heatwave day on which enhanced cloud cover over the forest was visible on satellite images. Two numerical experiments (large eddy simulations) with a homogeneous forest cover were performed, one in which the sensible heat flux was increased with approximately 5% of the net radiation (*Warm*) and another one in which the same amount of energy was added to the latent heat flux (*Wet*). The addition of energy to the sensible heat flux led to a stronger increase in cloud cover than the same addition to the latent heat flux, this difference was even more clear in the liquid water path.

The mean height difference between the boundary layer top and the lifting condensation level was similar for both experiments, the mean relative humidity (RH) at the boundary layer top (an often used indicator for cloud formation) showed little differences as well. The probability density distribution of RH at the boundary layer top however revealed the presence of two separate peaks, indicating that the mean provides insufficient information. Furthermore, it is remarkable to note that cloud formation already started at mean relative humidity values below 60%. This shows the importance of taking the frequency distribution of quantities such as RH into account, and thus stresses the need for using LES models to accurately predict cloud formation.

An analysis of why the cloud cover is higher in the *Warm* experiment suggests that the warming of the boundary layer leads to a decrease in the required amount of energy for air parcels to reach the lifting condensation level. The thermals also modify the virtual potential temperature profile above the boundary layer top, such that the required energy is further reduced.

As forests in West and Central Europe appear to have a higher sensible heat flux than crop- or grassland (Teuling et al., 2010), the results of our study indicate a mechanism of how cloud formation might be enhanced over these forests. However, the obtained results are case specific and should be extrapolated to other days and forest regions with caution. Additionally, it should be noted that the satellite images of that day showed deep convection developing over the forest, while our simulations only showed shallow cumulus convection. Mechanisms such as forest breezes might be responsible for this discrepancy. Future studies should quantify to what extent the cloud formation mechanism described in this study is responsible for the enhanced cloud cover visible over forests in France and potentially other regions in the world. For forest areas with a higher sensible heat flux than their surroundings (e.g. West and Central European forests), it would be interesting to quantify the temporal frequency of occurrence of atmospheric conditions which are favourable for preferential cloud formation over areas with a strong sensible heat flux. Other potential mechanisms for enhancing cloud formation over forests should also be a focus of future research.

Acknowledgements

Clouds and forests – two aspects of nature that interest me very much – came to meet in this thesis. I want to express a sincere word of thanks to my supervisor Chiel van Heerwaarden for the quick responses to my e-mails with questions, for offering me the possibility to work on this subject and for the help in steering this research in the right direction. Our meetings were always pleasant and provided a lot of insight in how to continue the research. I also want to thank Leo Kroon for his assistance in supervision in the beginning of this thesis project. Furthermore I want to thank my family for the emotional and logistical support.

Cover picture: cumulus clouds (picture from www.nandyradiotelephony.com)

References

Abbs, D., & Physick, W. L. (1992). Sea-breeze observations and modeling. *Austr. Meteor. Mag*, *41*, 7-19.

American Meteorological Society. (2012). Frictional convergence. Retrieved from http://glossary.ametsoc.org/wiki/Frictional_convergence on 26 July 2017.

Baldocchi, D., Falge, E., Gu, L., Olson, R., Hollinger, D., Running, S., ... & Wofsy, S. (2001). FLUXNET: A new tool to study the temporal and spatial variability of ecosystem–scale carbon dioxide, water vapor, and energy flux densities. *Bulletin of the American Meteorological Society*, *82*(11), 2415-2434.

Bannon, P. R. (1996). On the anelastic approximation for a compressible atmosphere. *Journal of the Atmospheric Sciences*, *53*(23), 3618-3628.

Benjamin, S. G., & Carlson, T. N. (1986). Some effects of surface heating and topography on the regional severe storm environment. Part I: Three-dimensional simulations. *Monthly weather review*, *114*(2), 307-329.

Beringer, J., Chapin, F. S., Thompson, C. C., & McGuire, A. D. (2005). Surface energy exchanges along a tundra-forest transition and feedbacks to climate. *Agricultural and Forest Meteorology*, *131*(3), 143-161.

Betts, A. (1973). Non-precipitating cumulus convection and its parameterization. *Quarterly Journal of the Royal Meteorological Society*, *99*(419), 178-196.

Blanchard, D. O. (1998). Assessing the vertical distribution of convective available potential energy. *Weather and Forecasting*, *13*(3), 870-877.

Bonan, G. B. (2008). Forests and climate change: forcings, feedbacks, and the climate benefits of forests. *science*, *320*(5882), 1444-1449.

Brown, A. R., Cederwall, R. T., Chlond, A., Duynkerke, P. G., Golaz, J. C., Khairoutdinov, M., ... & Neggers, R. A. J. (2002). Large-eddy simulation of the diurnal cycle of shallow cumulus convection over land. Quarterly Journal of the Royal Meteorological Society, 128(582), 1075-1093.

Cassiani, M., Katul, G. G., & Albertson, J. D. (2008). The effects of canopy leaf area index on airflow across forest edges: large-eddy simulation and analytical results. *Boundary-layer meteorology*, *126*(3), 433-460.

Chaboureau, J. P., Guichard, F., Redelsperger, J. L., & Lafore, J. P. (2004). The role of stability and moisture in the diurnal cycle of convection over land. *Quarterly Journal of the Royal Meteorological Society*, *130*(604), 3105-3117.

Couvreux, F., Hourdin, F., & Rio, C. (2010). Resolved versus parametrized boundary-layer plumes. Part I: A parametrization-oriented conditional sampling in large-eddy simulations. *Boundary-layer meteorology*, *134*(3), 441-458.

Costa, M. H., & Foley, J. A. (2000). Combined effects of deforestation and doubled atmospheric CO2 concentrations on the climate of Amazonia. *Journal of Climate*, *13*(1), 18-34.

Courant, R., Friedrichs, K., & Lewy, H. (1967). On the partial difference equations of mathematical physics. *IBM journal*, *11*(2), 215-234.

Dee, D. P., Uppala, S. M., Simmons, A. J., Berrisford, P., Poli, P., Kobayashi, S., ... & Vitart, F. (2011). The ERA-Interim reanalysis: Configuration and performance of the data assimilation system. *Quarterly Journal of the royal meteorological society*, *137*(656), 553-597.

Durieux, L., Machado, L. A. T., & Laurent, H. (2003). The impact of deforestation on cloud cover over the Amazon arc of deforestation. *Remote Sensing of Environment*, *86*(1), 132-140.

ECMWF: European Centre For Medium-Range Weather Forecasts. (no date) ERA-Interim http://www.ecmwf.int/en/research/climate-reanalysis/era-Interim, visited on 11/12/2016

Eder, F., De Roo, F., Rotenberg, E., Yakir, D., Schmid, H. P., & Mauder, M. (2015). Secondary circulations at a solitary forest surrounded by semi-arid shrubland and their impact on eddy-covariance measurements. *Agricultural and Forest Meteorology*, *211*, 115-127.

Ek, M. B., & Holtslag, A. A. M. (2004). Influence of soil moisture on boundary layer cloud development. *Journal of hydrometeorology*, *5*(1), 86-99.

Ek, M., & Mahrt, L. (1994). Daytime evolution of relative humidity at the boundary layer top. *Monthly Weather Review*, *122*(12), 2709-2721.

Fisch, G., Tota, J., Machado, L. A. T., Silva Dias, M. D., da F. Lyra, R. F., Nobre, C. A., ... & Gash, J. H. C. (2004). The convective boundary layer over pasture and forest in Amazonia. *Theoretical and Applied Climatology*, *78*(1), 47-59.

Gambill, L. D., & Mecikalski, J. R. (2011). A satellite-based summer convective cloud frequency analysis over the southeastern United States. *Journal of Applied Meteorology and Climatology*, *50*(8), 1756-1769.

Garcia-Carreras, L., & Parker, D. J. (2011). How does local tropical deforestation affect rainfall?. *Geophysical Research Letters*, *38*(19).

Garcia-Carreras, L., Parker, D. J., & Marsham, J. H. (2011). What is the mechanism for the modification of convective cloud distributions by land surface-induced flows?. *Journal of the Atmospheric Sciences*, *68*(3), 619-634.

Gentine, P., Bellon, G., & van Heerwaarden, C. C. (2015). A Closer Look at Boundary Layer Inversion in Large-Eddy Simulations and Bulk Models: Buoyancy-Driven Case. *Journal of the Atmospheric Sciences*, *72*(2), 728-749.

Gentine, P., Holtslag, A. A., D'Andrea, F., & Ek, M. (2013). Surface and atmospheric controls on the onset of moist convection over land. *Journal of Hydrometeorology*, *14*(5), 1443-1462.

Huang, H. Y., & Margulis, S. A. (2011). Investigating the impact of soil moisture and atmospheric stability on cloud development and distribution using a coupled large-eddy simulation and land surface model. *Journal of Hydrometeorology*, *12*(5), 787-804.

Khairoutdinov, M., & Randall, D. (2006). High-resolution simulation of shallow-to-deep convection transition over land. *Journal of the atmospheric sciences*, *63*(12), 3421-3436.

Lenschow, D. H., & Stephens, P. L. (1980). The role of thermals in the convective boundary layer. *Boundary-Layer Meteorology*, *19*(4), 509-532.

Mahrt, L., & Ek, M. (1993). Spatial variability of turbulent fluxes and roughness lengths in HAPEX-MOBILHY. *Boundary-Layer Meteorology*, *65*(4), 381-400.

Nair, U. S., Lawton, R. O., Welch, R. M., & Pielke, R. A. (2003). Impact of land use on Costa Rican tropical montane cloud forests: Sensitivity of cumulus cloud field characteristics to lowland deforestation. *Journal of Geophysical Research: Atmospheres*, *108*(D7).

Neggers, R. A. J., Jonker, H. J. J., & Siebesma, A. P. (2003). Size statistics of cumulus cloud populations in large-eddy simulations. *Journal of the atmospheric sciences*, *60*(8), 1060-1074.

Neggers, R. A. J., Siebesma, A. P., & Jonker, H. J. J. (2002). A multiparcel model for shallow cumulus convection. *Journal of the atmospheric sciences*, *59*(10), 1655-1668.

Negri, A. J., Adler, R. F., Xu, L., & Surratt, J. (2004). The impact of Amazonian deforestation on dry season rainfall. *Journal of Climate*, *17*(6), 1306-1319.

Pascal, M., Le Tertre, A., & Saoudi, A. (2012). Quantification of the heat wave effect on mortality in nine French cities during summer 2006. *PLoS currents*, *4*.

Rieck, M., Hohenegger, C., & van Heerwaarden, C. C. (2014). The influence of land surface heterogeneities on cloud size development. *Monthly Weather Review*, *142*(10), 3830-3846.

Seifert, A., & Beheng, K. D. (2001). A double-moment parameterization for simulating autoconversion, accretion and selfcollection. *Atmospheric research*, *59*, 265-281.

Shannak, B., Träumner, K., Wieser, A., Corsmeier, U., & Kottmeier, C. (2011). Flow characteristics above a forest using light detection and ranging measurement data. *Proceedings of the Institution of Mechanical Engineers, Part C: Journal of Mechanical Engineering Science*, 0954406211417944.

Shaw, R. H., & Schumann, U. (1992). Large-eddy simulation of turbulent flow above and within a forest. *Boundary-Layer Meteorology*, *61*(1-2), 47-64.

Shukla, J., Nobre, C., & Sellers, P. (1990). Amazon deforestation and climate change. Science(Washington), 247(4948), 1322-1325.

Sohngen, B., & Mendelsohn, R. (2003). An optimal control model of forest carbon sequestration. *American Journal of Agricultural Economics*, *85*(2), 448-457.

Sommeria, G., & Deardorff, J. W. (1977). Subgrid-scale condensation in models of nonprecipitating clouds. *Journal of the Atmospheric Sciences*, *34*(2), 344-355.

Souza, E. P., Rennó, N. O., & Silva Dias, M. A. (2000). Convective circulations induced by surface heterogeneities. *Journal of the atmospheric sciences*, *57*(17), 2915-2922.

Spracklen, D. V., Bonn, B. & Carslaw, K. S. (2008). Boreal forests, aerosols and the impacts on clouds and climate. Philos. Trans. R. Soc. A. 366, 4613–4626

Stevens, B., & Seifert, A. (2008). Understanding macrophysical outcomes of microphysical choices in simulations of shallow cumulus convection. *Journal of the Meteorological Society of Japan. Ser. II*, *86*, 143-162.

Teuling, A. J., Seneviratne, S. I., Stöckli, R., Reichstein, M., Moors, E., Ciais, P., ... & Wohlfahrt, G. (2010). Contrasting response of European forest and grassland energy exchange to heatwaves. *Nature Geoscience*, *3*(10), 722-727.

Teuling, A. J., Taylor, C. M., Meirink, J. F., Melsen, L. A., Miralles, D. G., van Heerwaarden, C. C., ... & de Arellano, J. V. G. (2017). Observational evidence for cloud cover enhancement over western European forests. *Nature Communications*, *8*, 14065.

Thompson, R. L., Mead, C. M., & Edwards, R. (2007). Effective storm-relative helicity and bulk shear in supercell thunderstorm environments. *Weather and forecasting*, *22*(1), 102-115.

Tompkins, A. M. (2002). A prognostic parameterization for the subgrid-scale variability of water vapor and clouds in large-scale models and its use to diagnose cloud cover. *Journal of the atmospheric sciences*, *59*(12), 1917-1942.

van Heerwaarden, C. C., & Vilà-Guerau de Arellano, J. (2008). Relative humidity as an indicator for cloud formation over heterogeneous land surfaces. *Journal of the Atmospheric Sciences*, *65*(10), 3263-3277.

van Heerwaarden, C. C., Vilà-Guerau de Arellano, J., Moene, A. F., & Holtslag, A. A. (2009). Interactions between dry-air entrainment, surface evaporation and convective boundary-layer development. *Quarterly Journal of the Royal Meteorological Society*, *135*(642), 1277-1291.

van Heerwaarden, C. C., Mellado, J. P., & De Lozar, A. (2014). Scaling laws for the heterogeneously heated free convective boundary layer. *Journal of the Atmospheric Sciences*, *71*(11), 3975-4000.

van Heerwaarden, C. C., & Mellado, J. P. (2016). Growth and decay of a convective boundary layer over a surface with a constant temperature. *Journal of the Atmospheric Sciences*, *73*(5), 2165-2177.

van Heerwaarden, C.C., van Stratum B.J.H., Heus, T., Gibbs, J.H. & Fedorovich, A. (2017). MicroHH 1.0: a computational fluid dynamics code for direct and large-eddy simulation of atmospheric boundary layer flows. Manuscript submitted for publication

Vilà-Guerau De Arellano, J., van Heerwaarden, C. C., & Lelieveld, J. (2012). Modelled suppression of boundary-layer clouds by plants in a CO2-rich atmosphere. *Nature geoscience*, *5*(10), 701.

Wang, J., Chagnon, F. J., Williams, E. R., Betts, A. K., Renno, N. O., Machado, L. A., ... & Bras, R. L. (2009). Impact of deforestation in the Amazon basin on cloud climatology. *Proceedings of the National Academy of Sciences*, *106*(10), 3670-3674.

Weckwerth, T. M. (2000). The effect of small-scale moisture variability on thunderstorm initiation. *Monthly weather review*, *128*(12), 4017-4030.

Wilde, N. P., Stull, R. B., & Eloranta, E. W. (1985). The LCL zone and cumulus onset. *Journal of climate and applied meteorology*, *24*(7), 640-657.

Williams, A. G., & Hacker, J. M. (1992). The composite shape and structure of coherent eddies in the convective boundary layer. *Boundary-Layer Meteorology*, *61*(3), 213-245.

Appendix A

List of symbols and abbreviations

c_p = specific heat capacity of air at constant pressure (1005 J $kg^{-1}K^{-1}$)

g = gravitational acceleration (9.81 ms^{-2})

L_v = latent heat of vaporisation water (2,5 * 10^6 J kg^{-1})

q_l = liquid water content (kg kg^{-1})

q_v = vapour specific humidity (kg kg^{-1})

q_t = total specific humidity, vapour + liquid water (kg kg^{-1})

q_s = saturated specific humidity (kg kg^{-1})

θ_l = liquid water potential temperature (K)

θ = potential temperature (K)

θ_v = virtual potential temperature (K)

T = absolute temperature (K)

T_v = virtual potential temperature (K)

CIN_{LCL} = condensation inhibition (J kg^{-1})

u = zonal component wind (m s^{-1})

v = meridional component wind (m s^{-1})

ug = zonal component geostrophic wind (m s^{-1})

vg = meridional component geostrophic wind (m s^{-1})

w = vertical velocity (m s^{-1})

z = height above model surface (m)

LCL = lifting condensation level

LFC = level of free convection

PBL = planetary boundary layer

LES = large eddy simulation

RH = relative humidity

LT = local time

Appendix B

Imposed geostrophic wind forcing and large scale advection

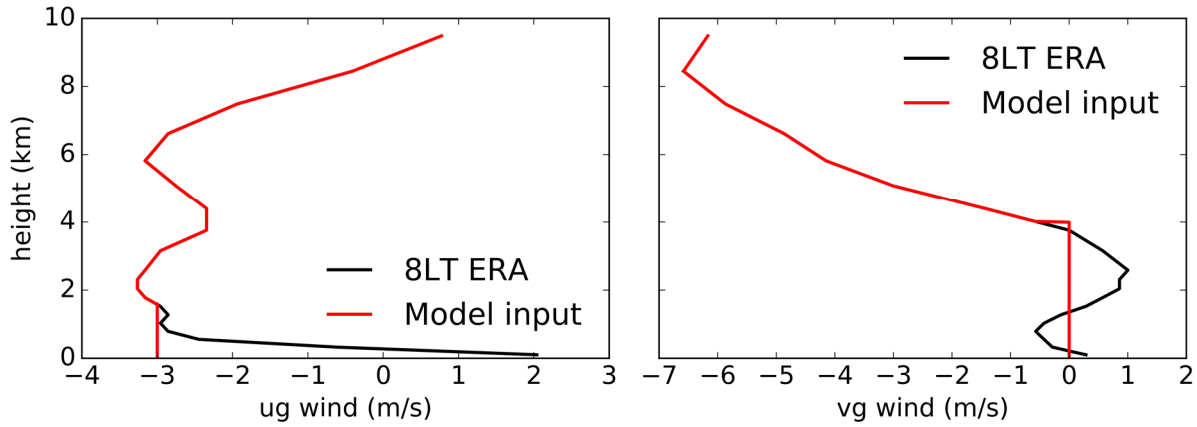

Figure B1: ERA-Interim geostrophic wind calculated from geopotential gradients (black line) and geostrophic wind profiles entered in the model (red line). The left graph is for the zonal component *ug*, the right graph shows the meridional component *vg*.

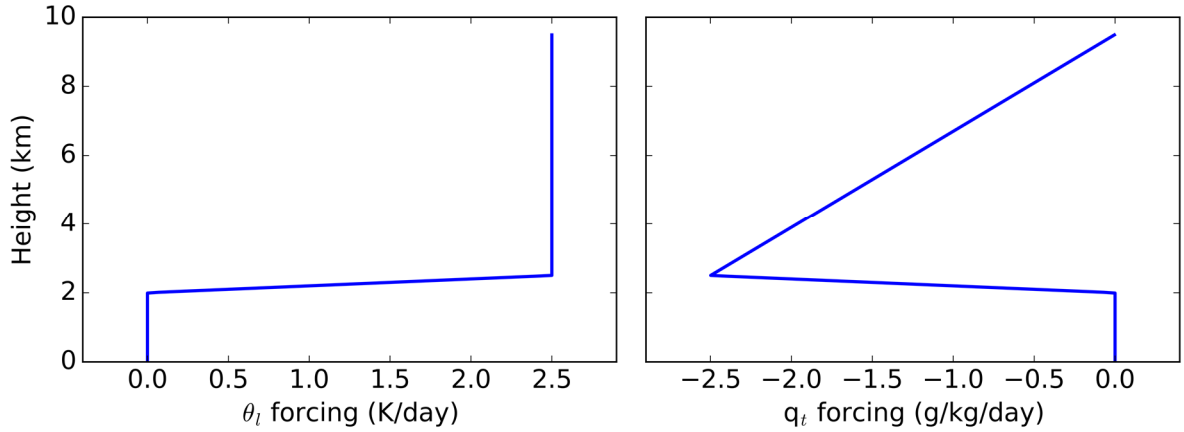

Figure B2: Prescribed large scale liquid water potential temperature (θ_l) and specific humidity (q_t) forcings. This represents large scale advection.

Appendix C

Details of model setup

Grid

Second order spatial discretisation

Advection

Advection scheme: second order

Subgrid model

Smagorinsky constant = 0.23
Maximum diffusion number for numerical scheme = 0.1
Turbulent Prandtl number = 1/3

Thermodynamics

Moist thermodynamics used (θ_l and q_t)

Boundaries

Flux scalar boundary condition at bottom, Neumann at top
q_t and θ_l gradients at the top derived from ERA-Interim:
θ_l gradient at top = 3,031 * 10^{-3} K m^{-1}
q_t gradient at top = -1.895 * 10^{-7} kg kg^{-1} m^{-1}
Roughness lengths heat and momentum = 1 m

Damping layer

Damping frequency = 2.23*10^{-3} s^{-1}, exponent = 2
Reference profile of damping layer updated in time

Initial perturbations

θ_l perturbations amplitude = 0.1 K
q_t perturbations amplitude = 0.1 g kg^{-1}
Those perturbations decay exponentially with height (exp = 2) and do not extend beyond a height of 200m. The number of their random seed = 2

Time integration

Selected numerical time integration: Runge-Kutta 3rd-order accuracy, 3 steps

Pressure

Second order pressure solver (tridiagonal solver)

Statistics

Sampling time 300 or 180 seconds, depending on run.

Large scale forcings

Coriolis parameter = 0.00010177 s^{-1}
Large scale vertical velocity = 0 m s^{-1}

Model version

MicroHH git-hash: 1.6.0-99-g5d6a8c2-dirty

Appendix D

Additional model output

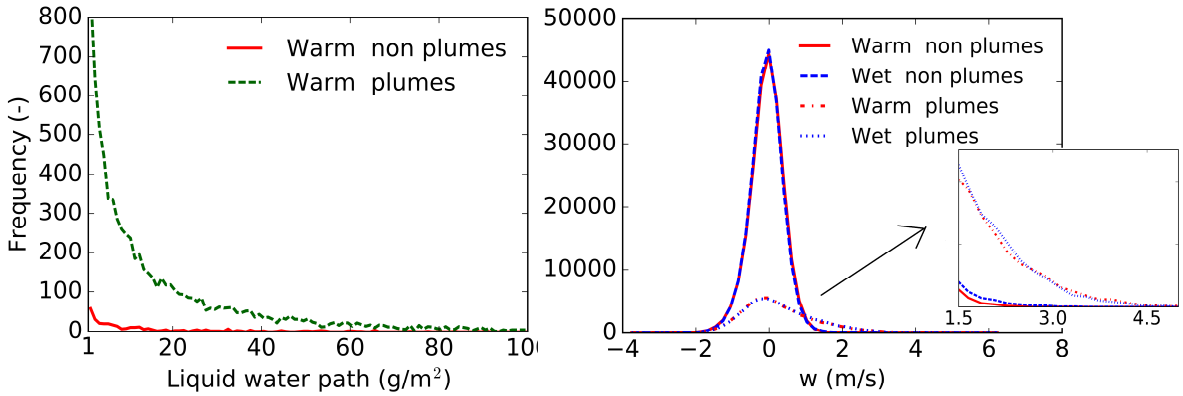

Figure D1: Frequency distribution of liquid water path (a), conditionally sampled by defining the 20% least buoyant cells as plumes. (b) shows the frequency distribution of the vertical velocity (w), with the inset picture focusing on the larger values of vertical velocity.

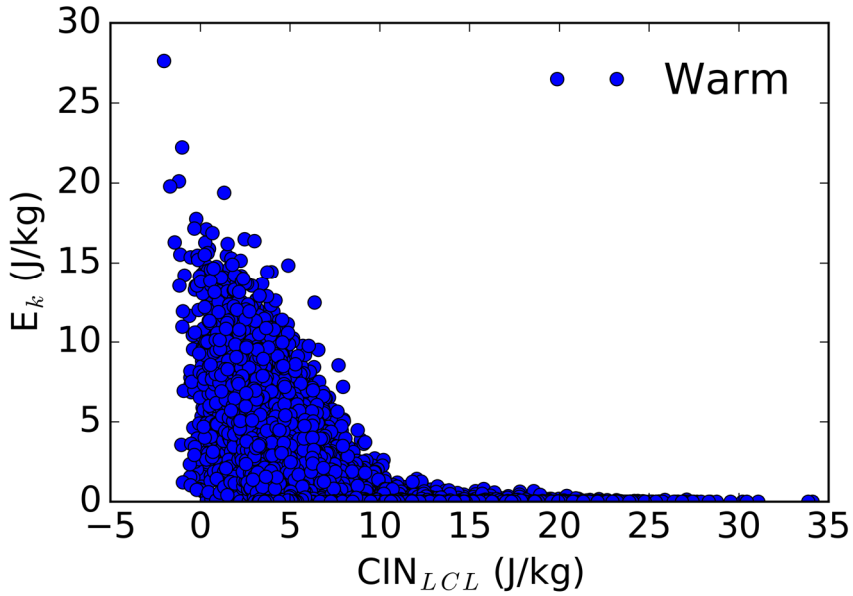

Figure D2: Scatterplot of CIN_{LCL} (calculated from a cross section at 2000 m) and E_k for the *Warm* run at 18 LT. Note that all cells with a negative vertical velocity were assigned zero kinetic energy.

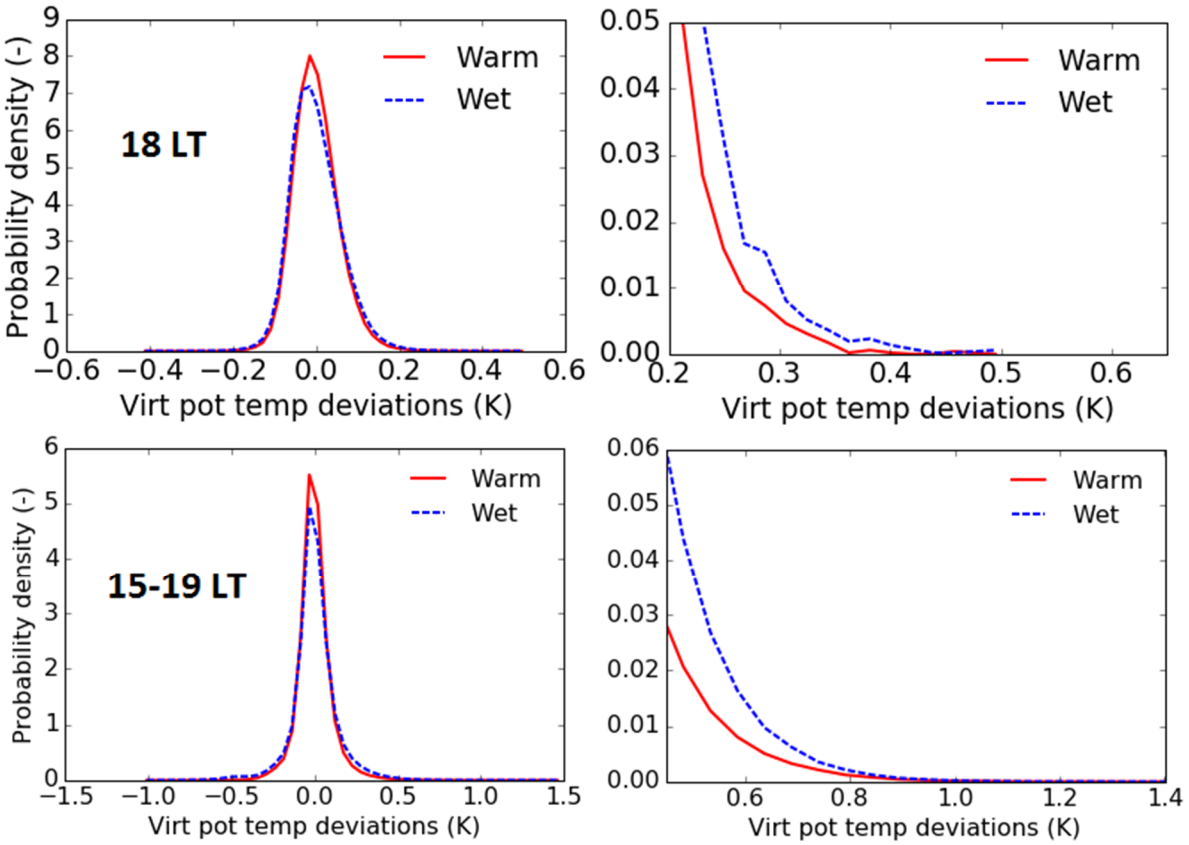

Figure D3: virtual potential temperature deviations for a cross section at 2000m. (a) shows the data for 18 LT, (b) zooms in on this plot to show the positive values more clearly. In (c) data is sampled every 30 mins from 15 LT to 19 LT. (d) zooms in on this plot to show the positive values more clearly

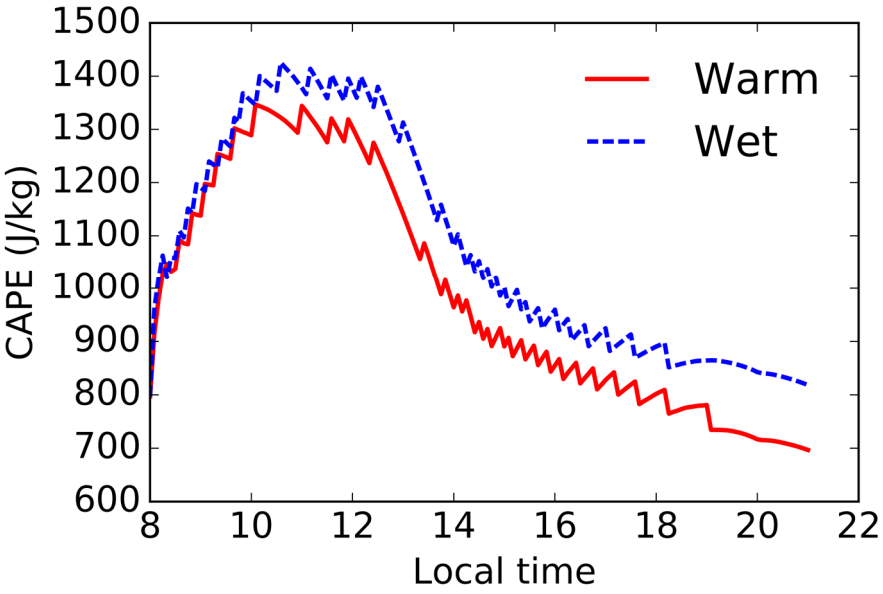

Figure D4: Surface based convective available potential energy (CAPE) for the *Warm* and *Wet* runs

Appendix E

Assumptions when using mean relative humidity

For ease of notation let q_v = a and q_s = b. Than the definition of RH in our study becomes:

$$\frac{a}{b} = \frac{\bar{a} + a'}{\bar{b} + b'} = \frac{\bar{a} + a'}{\bar{b} + b'} * \frac{\bar{b} - b'}{\bar{b} - b'}$$

$$\frac{a}{b} = \frac{\bar{a}\bar{b} - \bar{a}b' + a'\bar{b} - a'b'}{(\bar{b})^2 - (b')^2}$$

where the overbar denotes a horizontal mean and the prime represents the deviation from this mean value.

if $(\bar{b})^2 \gg (b')^2$:

$$\frac{a}{b} = \frac{\bar{a}}{\bar{b}} - \frac{\bar{a}b'}{(\bar{b})^2} + \frac{a'}{\bar{b}} - \frac{a'b'}{(\bar{b})^2}$$

And thus

$$\text{mean}\left(\frac{a}{b}\right) = \frac{\bar{a}}{\bar{b}} - \frac{\overline{a'b'}}{(\bar{b})^2}$$

If there is no correlation, than the mean of $\left(\frac{a}{b}\right) = \frac{\bar{a}}{\bar{b}}$

Equating the mean of RH to the mean of q_v divided by the mean of q_s thus requires two assumptions.